SUSCEPTIBILITY OF QUADCOPTER FLIGHT TO TURBULENCE

A Thesis

Presented to the Faculty of the Graduate School

of Cornell University

in Partial Fulfillment of the Requirements for the Degree of

Master of Science

by

Joshua Vincent Solberg

August 2018

ABSTRACT

Quadcopters are used in a wide variety of applications, almost all of which require flying in turbulent conditions. Especially for small quadcopters, whose velocities are of the same order as those of the velocity fluctuations caused by wind or proximity to obstacles, understanding the effects of turbulence is of vital importance in developing better control and design strategies. To this end, an experiment was designed and conducted in a wind tunnel to systematically analyze the susceptibility of small quadcopter flight to disturbances due to homogeneous turbulence. A framework relating turbulence properties and this susceptibility was developed and compared to experimental results. The initial results are found to agree with this framework, and are used to develop a plan for future experiments.

BIOGRAPHICAL SKETCH

Joshua Solberg graduated with a BS in Mechanical Engineering from Loyola Marymount University in 2016. While there, he worked on research projects relating to turbine blade film cooling and hydrogen fusion. In the summer of 2017, he interned for Solar Turbines in their Heat Transfer division. He is an Eagle Scout, and enjoys backpacking, cooking, and listening to and performing classical music.

To my grandfathers, Gerald and Vincent, whose hard work and kindness inspire me daily.

ACKNOWLEDGEMENTS

I would like to extend the sincerest gratitude to everyone who has helped me through my graduate school journey.

I would like to thank my advisor Gregory Bewley for his guidance and support through this whole process, without which this project would not have been possible.

I would also like to thank my labmates Kevin Benson, Chris Draikiwicz, Dasha Gloutak, Reece Kearney, Kasey Laurent, and Naoki Manzano, as well as all my fellow graduate students, for helping to make this experience more fun than I ever imagined.

For their unwavering love and support, I have the profoundest gratitude for my parents, Bryon and Bernadette, and my brother Garrett.

Finally, I would like to thank Cornell University and the Sibley School of Mechanical Engineering for providing me with this incredible opportunity.

TABLE OF CONTENTS

CHAPTER 1

INTRODUCTION

When the Wright brothers searched for a site to attempt the first powered human flight, they were looking for a place with the conditions that could provide any possible advantage to their experimental aircraft. They settled on a beach in Kitty Hawk, North Carolina, whose constant, fast wind they hoped would provide a boost in lift that would give them the best chance of success [1]. Yet, as the jittery nature of their first flight showed, however constant the wind seemed there is no such thing as a truly steady wind. Even wind of a constant velocity is still inherently unsteady due to the turbulent nature of the atmospheric boundary layer, and therefore, any flight that takes place in earth's atmosphere will be subject to the effects of this unsteadiness [2].

Especially as smaller and smaller aircraft are becoming commonplace, understanding how turbulence affects the flight of quadcopters is of vital importance. For many different types of civilian and military applications, small quadcopters are being used due to their simplicity and ease of use. However, as these types of aircraft decrease in size, their velocities decrease to the same scales as turbulent fluctuations [3]. In addition, their power capacity similarly decreases based on the size of the battery they are able to carry [4]. By understanding the effects of turbulence at these scales on small quadcopters and the types of factors that make them more or less susceptible to these effects, control and design strategies can be employed to not only increase the efficiency of quadcopter flight in the atmosphere, but also enable longer missions in more turbulent environments that would not otherwise have been possible.

The problems facing quadcopters and other small aircraft in turbulence have been known for some time. Conventional aircraft fly in a regime of Reynolds numbers greater than 10^5, where aerodynamic forces such as lift and drag are well studied [3]. However, as shown in Figure 1.1, small aircraft fly more slowly and are subject to a different regime of aerodynamic forces than conventional aircraft. Below Reynolds numbers of 10^5, lift and drag are affected by much more complex phenomena, since separation, transition, and reattachment can occur on the same length scales as those of the rotors [5]. Understanding the flight of quadcopters with respect to turbulence therefore requires understanding the effects of phenomena on both large and small scales.

To connect the effects of these regimes, investigations have been made into the effects on quadcopter flight of frame drag when subjected to wind disturbances [7] and the the effects of the interaction of propellers with wind [8]. A body of work also exists that specifically explores quadcopter dynamics and control when subjected to wind disturbances [9][10][11][12]. Most works that pertain to control of quadcopters in these contexts, simulation and experimental alike, have treated turbulence and wind as disturbances to reject [8]. However, an important area of research going forward relates to finding ways to exploit the energy present in turbulent flows.

For small fixed wing unmanned aircraft, a large body of work exists in this regard. Using the flight of birds as inspiration, the ability to use thermal updrafts to aid in the endurance of unmanned aircraft has been demonstrated by Boslough [13], Allen [14], Langelaan [15], and Lawrance [16]. The exploitation of atmospheric turbulence in the form of wind gusts using dynamic control systems has also been explored [17][18]. Exploiting turbulence within thermal up-

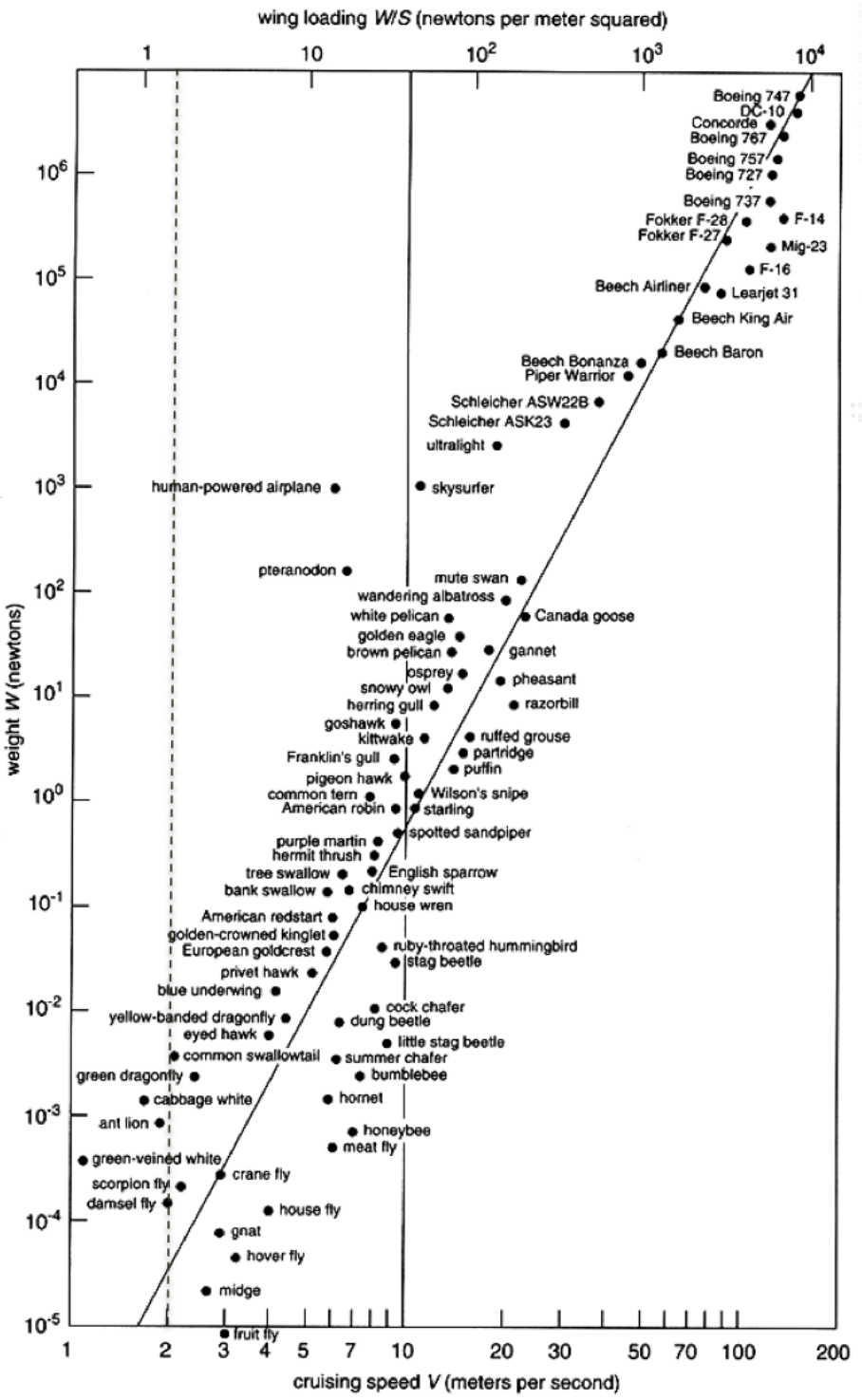

Figure 1.1: Great Flight Diagram [3]. A line marking $10m/s$ is shown, along with a dashed line for u' for a representative atmospheric turbulence intensity of 20% [6].

drafts has also been investigated using machine learning [19]. To aid unmanned vehicles in exploiting energy in the atmosphere, work has been done to use onboard sensors to estimate wind fields [20]. When it comes to quadcopters, however, such work is missing. For one, the aerodynamics of quadcopters are different than those of fixed wing unmanned aircraft, particularly in terms of the inability of quadcopters to glide [8]. Quadcopters are also expected to fly in different environments, such as urban settings or closely packed swarms [3]. Extending and applying the results of previous work to quadcopters therefore requires an understanding of the effects of turbulence specific to quadcopters.

Therefore, in order to understand how to exploit turbulence for the purposes of more efficient quadcopter flight, a fundamental understanding is needed with respect to exactly how turbulence affects quadcopters and which properties of turbulence and the quadcopter itself are responsible for those effects. A wide range of parameters are relevant, such as the properties of the turbulence (e.g. velocity, time scales, length scales, intermittent effects), the size of the quadcopter, and the control scheme [3][10][12]. Determining the effects of these different parameters requires isolating them as much as possible. By experimentally testing very small quadcopters flying under the command of a simple control scheme in very tightly controlled homogeneous turbulent flows, this project seeks to provide a framework for quantifying how susceptible quadcopters are to the effects of these different parameters. After providing the basis for this framework, future investigations are proposed to make the framework more comprehensive and to investigate questions left unanswered.

CHAPTER 2

TURBULENCE

Turbulence refers to flows characterized by unsteady and chaotic changes in velocity and pressure with both position and time. Turbulence is a three-dimensional phenomenon, and is composed of rotational structures known as eddies. The Reynolds number, or ratio of inertial to viscous forces within the flow, for turbulence is typically high, though the Reynolds number at which the transition from laminar to turbulent flow occurs depends on the situation. To analyze and describe the chaotic, multi-scale behavior of turbulence, statistical tools have been developed, several of which will be discussed below [2].

2.1 Terminology

In this investigation, a few terms relating to turbulence are of particular importance. The first is U, which is the time average of velocity, or mean wind speed. The second is u', which is the root mean square of velocity fluctuations relative to the mean, which quantifies the strength of the turbulent fluctuations. These two terms together can be used to express the relative strength of the velocity fluctuations, known as turbulence intensity [2]:

$$T.I. = \frac{u'}{U} \tag{2.1}$$

A velocity signal from a measurement recorded during this project is shown in Figure 2.1.

An important property of the turbulent velocity is that it is correlated in time and space. Using Taylor's hypothesis, or the assumption that the advection of

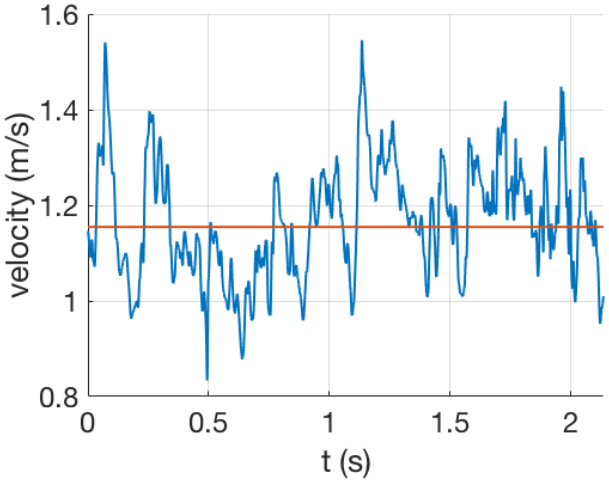

Figure 2.1: Velocity signal excerpt of a turbulent flow of 13% intensity used in this experiment. This flow was generated using an active grid in a wind tunnel during the course of this project. More specifics regarding the active grid, the wind tunnel, and the velocity measurement techniques are in section 3.6.

turbulent structures is entirely due to the mean flow, temporal measurements can be converted to spatial ones by

$$x = t \times U \tag{2.2}$$

This assumption is generally valid when $u'/U \ll 1$ [2]. The correlation of turbulent velocity can be quantified by the autocorrelation function (ACF) f due to spatial separation, which is defined as

$$f(\Delta x) = \frac{\langle u'(x)u'(x+\Delta x)\rangle}{\langle u'^2\rangle} \tag{2.3}$$

Where x is position and Δx is spatial separation [2]. Another measure of this correlation is the integral length scale, which is calculated by integrating under the spatial autocorrelation function (Figure 2.2) [2]. This length scale corresponds to the the size of the largest eddies in the flow, and is calculated by

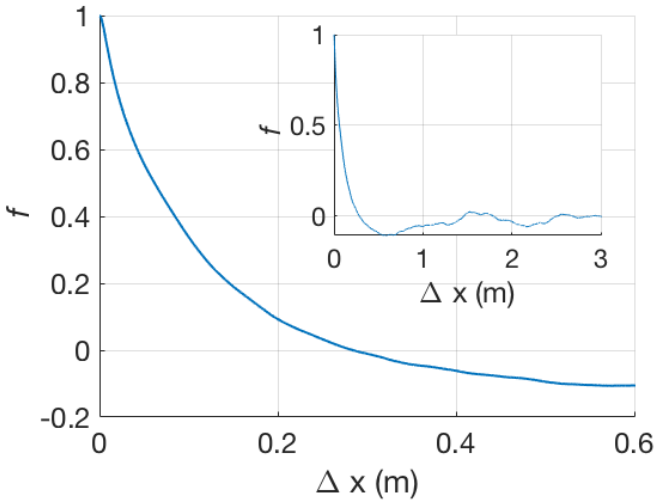

Figure 2.2: Autocorrelation Function (ACF) f of turbulent velocity vs. spatial separation for flow whose excerpt is in Figure 2.1. The inset shows the ACF over a longer spatial domain. Time measurements can be converted to spatial ones using Taylor's hypothesis, $\Delta x = \Delta t \times U$, which is generally valid when $u'/U \ll 1$ [2].

$$L = \int_0^\infty f(r)dr \tag{2.4}$$

where r is spatial separation [2]. However, since the autocorrelation function oscillates about 0 , integrating to infinity resulted in $L = 0$. To rectify this, the domain of integration was taken to be from $\Delta x = 0$ until the first time the autocorrelation function crossed 0.

The largest eddies in a turbulent flow are where kinetic energy enters the flow, and constitute what is known as the energy injection range [2]. Energy from the energy injection range is passed down to eddies of progressively smaller and smaller sizes until it is dissipated in the form of heat due to viscosity [21]. The energy content across the length scales of a turbulent flow can be analyzed using the turbulent kinetic energy spectrum, an example of which is shown in Figure 2.3. To calculate the energy spectrum, the velocity signal is

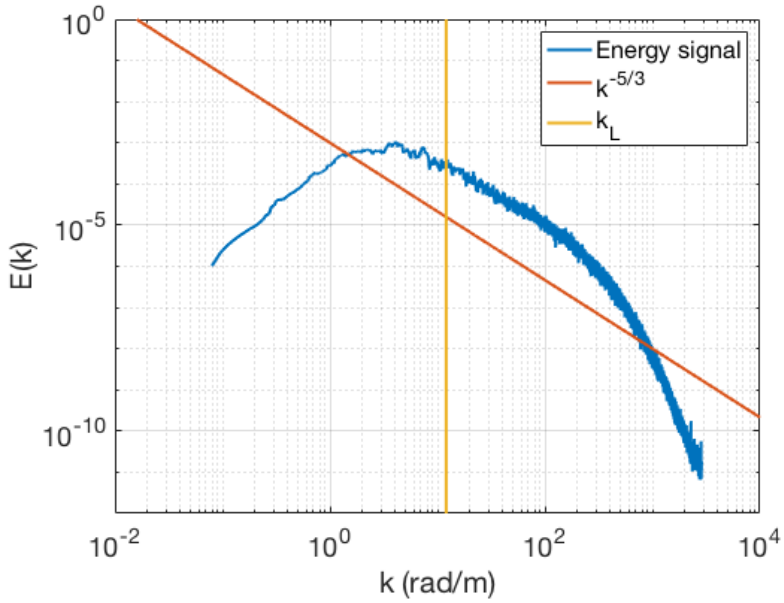

Figure 2.3: Turbulet Kinetic Energy spectrum for the signal whose excerpt is shown in Figure 2.1. The $-5/3$ power law and the location of integral scale are shown for comparison [2].

converted to the frequency domain using a Fourier transform, and frequency is then converted to wavenumber by

$$k = \frac{2\pi f}{U} \tag{2.5}$$

where f is frequency in Hertz. The spectrum is normalized to satisfy Parseval's Theorem, meaning that

$$\int_0^\infty E(k)dk = \left\langle (u')^2 \right\rangle \tag{2.6}$$

Where $E(k)$ is the energy spectrum [2]. The spectrum signal was smoothed using a moving average filter to remove noise.

Homogeneous turbulence refers to turbulence for which the average characteristics are independent of position within the fluid [2]. This property was desirable, since by flying the quadcopters at fixed positions in the wind tun-

nel, the properties of the turbulence affecting the quadcopter could be assumed to be uniform for the entirety of a given flight. In designing this experiment, turbulent intensities and length scales were varied from as small to as large as possible given the constraints of the tools available in the laboratory. The lower limit on turbulence intensity was approximately 0.75%, and the upper limit was approximately 13%. Integral length scales varied from 3.3 to 8.8cm. These limits were set by the wind speeds the quadcopters could fly at and the turbulence generation tools described in section 3.6.

2.2 Model of Quadcopter Displacement in Turbulence

As an initial guide to this exploration, a theoretical framework was developed from dimensional arguments to provide a way to quantify the susceptibility of a quadcopter to turbulence as well as to predict which parameters would be relevant.

Consider a quadcopter of mass m and cross-sectional area A in a turbulent flow of mean velocity U, that is displaced a distance Δh by a turbulent gust with some characteristic length L^* and a velocity u^* (Figure 2.4). The acceleration of the quadcopter during the displacement scales as

$$a \sim \frac{\Delta h}{\tau^2} \tag{2.7}$$

where the time scale τ is the eddy interception time, or the amount of time the gust has to affect the quadcopter before being swept past by the mean flow, given by

$$\tau = T_e \approx \frac{L^*}{U} \tag{2.8}$$

The acceleration then can be expressed as

$$a \sim \Delta h \left(\frac{U}{L^*} \right)^2 \tag{2.9}$$

Assuming that this displacement is caused only by the effects of drag on the body of the quadcopter, a force balance can be performed:

$$F_d = \frac{1}{2} C_d \rho A u^{*2} \tag{2.10}$$

$$F_d = ma \sim m \Delta h \left(\frac{U}{L^*} \right)^2 \tag{2.11}$$

where F_d is the drag force, C_d is the drag coefficient, and ρ is the density of the fluid. The displacement can then be expressed as

$$\Delta h \sim \frac{1}{2} \frac{\rho A L^{*2}}{m} C_d \left(\frac{u^*}{U} \right)^2 \tag{2.12}$$

Instead of measuring individual displacements and gust velocities, these quantities can be expressed and measured statistically. The statistical measure for displacement is taken as the standard deviation of position x, or

$$\Delta h \Rightarrow \left\langle x^2 \right\rangle^{1/2} \tag{2.13}$$

and the statistical measure of characteristic velocity of the gust as the root mean square velocity of the turbulence, or

$$u^* \Rightarrow u' \tag{2.14}$$

Using the statistical terms to replace their respective terms in equation (2.12), the scaling relation can be re-expressed in terms of an equality:

$$\frac{\left\langle x^2 \right\rangle^{1/2}}{L^*} = C \left(\frac{\rho A L^*}{m} \right) \left(\frac{u'}{U} \right)^2 \tag{2.15}$$

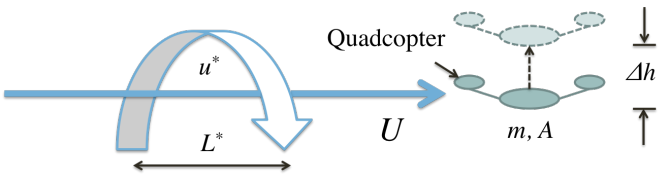

Figure 2.4: Quadcopter displacement when subjected to a turbulent gust, in the frame of the quadcopter

The right hand term $\rho AL^*/m$ represents the ratio of the mass of the column of air that affects the quadcopter to the mass of the quadcopter itself. The term u'/U is the turbulence intensity, and the coefficient C represents a measure of the susceptibility of the quadcopter to displacement due to turbulence, and combines information such as the drag coefficient (C_D) and the effect of feedback control.

CHAPTER 3

EXPERIMENTAL SETUP

3.1 System Architecture

A closed-loop system was constructed so that a quadcopter could be flown in the wind tunnel without requiring human input. A schematic is shown in Figure 3.1. A camera was used to acquire images of the quadcopter, which an image-processing algorithm converted into position information. This position information was then used as the input for a control algorithm to determine the appropriate commands to send the the quadcopter, which were delivered using a wireless transceiver. The workings of each of these components are discussed in detail below.

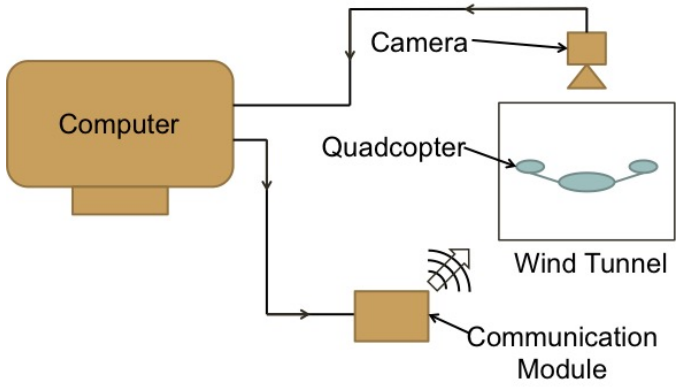

Figure 3.1: System Architecture for autonomous flight of quadcopter in a wind tunnel. A camera acquires images of the quadcopter, which are used by the computer to determine the quadcopter's position and the necessary flight commands. These commands are sent to the quadcopter using a wireless communication module. More details regarding each component are given below.

3.2 Quadcopter Selection

The first key decision that had to be made when designing this experiment was the selection of a quadcopter. A major consideration for this decision was size. To limit the effects of the quadcopter's propeller wakes interacting with the wind tunnel walls and the flow, a small quadcopter relative to the size of the wind tunnel was preferred. A small quadcopter would also be smaller relative to the structures within the turbulent flows generated by the wind tunnel, allowing for the analysis of the effects of length scales on the same order as its length.

A second consideration was the sophistication of the quadcopter's internal electronics. More expensive quadcopters, particularly those intended for use with on-board cameras, tend to contain sophisticated automatic stabilization protocols, which would operate independently from and potentially interfere excessively with external control algorithms. So, for this project, a cheaper quadcopter, with the bare minimum of internal control, was desired. Working from these considerations, the quadcopter selected for this project was the Cheerson CX-10 Mini, which along with its controller can be seen in Figure 3.2. The physical specifications for this quadcopter can be seen in Table 3.1.

Due to the short flight time and fragility of this type of quadcopter, a fleet of 16 quadcopters was used over the course of this project. For identification purposes, each individual quadcopter was named after a type of bird. The six quadcopters that survived until the end of this project were dubbed Puffin, Sparrow, Magpie, Finch, Swift, and Robin.

Figure 3.2: Cheerson CX-10 and Controller (Coin for scale)

Table 3.1: Cheerson CX-10 Specifications. The dimensions refer to the distances between the edges of the airframe and the distance between where the quadcopter rests on the ground and the top of the propeller axles, respectively.

Weight:	12g
Dimensions:	40x40x22mm
Lipo Battery:	3.7V 100mAh
Flight Time:	3-5 minutes
Max Speed:	$\approx 4m/s$

3.3 Quadcopter Communication

As outlined in section 3.1, a method was needed to relay commands from the flight control algorithm on the computer directly to the quadcopter. The Cheerson CX-10 is controlled with a 4-channel 2.4GHz radio transmitter, which converts the instructions from the controllers joysticks into Pulse Position Modulation (PPM) signals that can be interpreted by the quadcopter. To fly the quadcopter without the controller, a setup was constructed that was able to masquerade as the original controller by converting the output of the control algorithm directly into PPM signals and transmitting them wirelessly to the quadcopter.

A search of open source quadcopter projects uncovered a way to communicate with the Cheerson CX-10 [22]. This setup operated on an Arduino Uno microcontroller, to which a 2.4GHz wireless transceiver module was wired (Figure

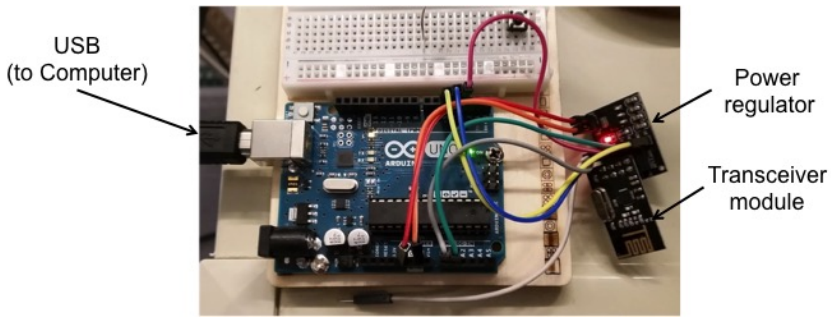

Figure 3.3: Arduino Uno Microcontroller with nRF24L01+ 2.4GHz wireless transceiver

3.3). Some open source Arduino code re-created the communication protocol of the original controller to allow for the Arduino to bind with the quadcopter, and, when connected to the computer through a serial connection, converted the instructions from the control algorithm into Pulse Position Modification (PPM) signals to be transmitted by the antenna [22]. The PPM signal for each channel consisted of an integer value between 1000 (minimum) and 2000 (maximum).

3.4 Quadcopter Control

3.4.1 Control Overview

Due to the nature of the quadcopter's internal electronics, control was limited to the degrees of freedom governed by the original controller, and could not be done by altering the rotational speeds of the quadcopters propellers individually. These degrees of freedoms and the names of the channels that control each one can be seen in Table 3.2. This limitation somewhat restricted control by adding another layer of control between the control algorithm and the behavior of the quadcopter itself, but it also simplified it. Since the quadcopter's

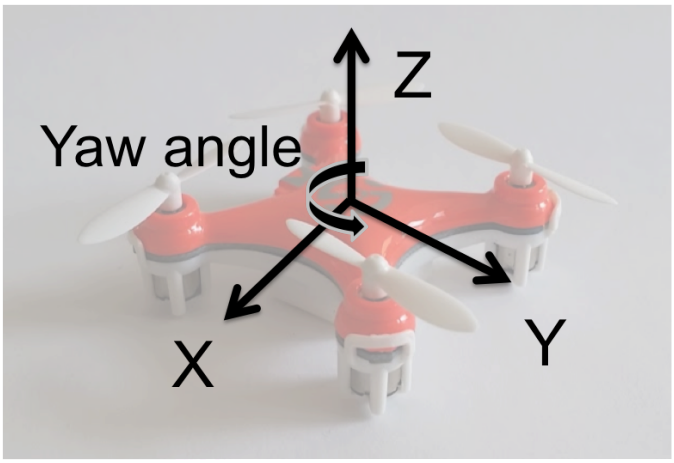

Figure 3.4: Degrees of freedom of quadcopter control

Table 3.2: Degrees of Freedom and Command Names

Degree of Freedom	Command name
Z	Throttle
X	Aileron
Y	Elevator
Yaw angle	Rudder

internal gyroscopes automatically kept its attitude stable, only the position of the quadcopter had to be considered when designing the control algorithm.

Each degree of freedom was controlled independently and simultaneously using a Proportional-Integral-Derivative (PID) controller. A PID controller operates using a continuously calculated value of error $e(t)$, which is the difference between the measured value of the variable being controlled, also known as the Process Variable (PV), and the desired value for that process variable, typically called the setpoint. The value of $e(t)$ is then used to calculate a correction signal $u(t)$ for the system being controlled, known as the plant, based on Proportional, Integral, and Derivative terms given by

$$u(t) = K_p e(t) + K_i \int_0^t e(t')dt' + K_d \frac{de(t)}{dt} \tag{3.1}$$

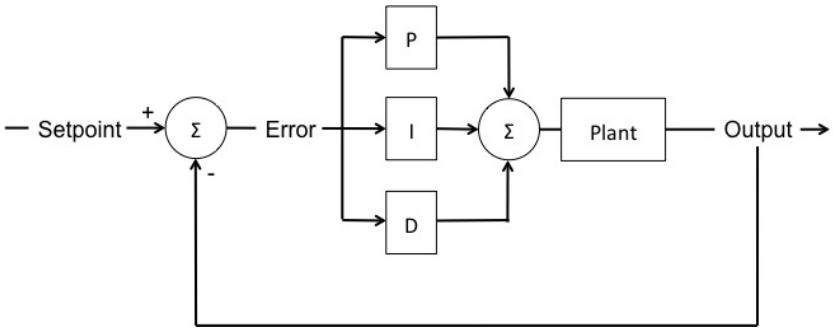

Figure 3.5: Block Diagram for PID controller. The value of the process variable (output) for the system being controlled (plant) is measured and compared to the desired value (setpoint). The difference between the output and the setpoint (error) is used to calculate a command signal by summing the proportional (P), integral (I) and derivative (D) terms from equation (3.1). The output is measured again and fed back into the loop.

Where K_p, K_i, and K_d are the known as the proportional, integral, and derivative gains, respectively. A block diagram for a PID controller is shown in Figure 3.5 [23].

This method of control is widely applicable, and was selected because of the simplicity of its design. However, while the implementation of this type of controller is straightforward, the process of determining the specific values for the PID gains for a given system, known as tuning, is not. Several iterations of design were necessary before the algorithm was robust enough to perform experiments in the wind tunnel.

3.4.2 Controller Tuning

Before the quadcopter could be flown in a turbulent flow, a few intermediate objectives had to be attained. The first of these was hovering in place in a quiescent flow. The process of achieving this objective involved a good deal of trial and error. A major challenge involved was that the interaction of the quadcopter's

propeller wake with the ground meant that any attempts at observing the effects of tuning changes could only be made away from the ground. Additionally, since the quadcopter was light and responsive to very small perturbations, efforts to tether the quadcopter in place even with very light string interfered significantly. To make matters yet more difficult, air circulation from the climate control in the lab added another layer of disturbances, requiring strategic barricades to be erected to shelter the test area. Nevertheless, once trial and error had produced a tuning configuration with proper gain scheduling that allowed the quadcopter to take off and then hover within the field of view of the camera, a more robust tuning procedure could be applied.

The first method of tuning that was applied was the Ziegler-Nichols (Z-N) method [23]. This method consists of first experimentally finding a proportional gain that when applied to the system produces oscillations of constant amplitude (i.e. $K_p = K_U, K_i = K_d = 0$). This gain and the period of the oscillations (T_U) are then used to directly compute the values of K_p, K_i, and K_d from a table. This method makes some simplifying assumptions regarding the nature of the system being controlled that almost certainly were not true of the quadcopter, but applying this procedure did produce a set of PID gains that allowed the quadcopter to hover until the batteries died [23]. However, when the quadcopter was subjected to the very light wind of a desk fan and crashed immediately, it was judged that the response time of the quadcopter using the gains determined by Z-N was too slow to even attempt flight in the wind tunnel.

Instead of returning to the time consuming and imprecise process of trial and error, an investigation was first made to understand and quantify how each degree of freedom was affected by the command responsible for controlling it.

By formulating a mathematical model approximating the behavior of the quadcopter, system performance characteristics such as rise time, settling time, and overshoot for a given controller tuning could be predicted virtually instantaneously using software tools. To this end, each degree of freedom was tested and modeled using transfer functions, which are mathematical functions that relate the output of a system to the input.

To determine the transfer function for each of the quadcopters' degrees of freedom, the assumption was made that each could be modeled as a second order system. This assumption means that the relationship between the input to a system and its corresponding output can be formed using only two properties: the natural frequency ω_n, which is the frequency at which the system will oscillate in the absence of an external force, and the damping ratio ζ, which is a measure of how oscillations of the system decay after being subjected to a disturbance [23]. Once these two parameters have been determined, the transfer function $G(s)$ can then be written as

$$G(s) = \frac{\omega_n^2}{s^2 + 2\zeta\omega_n s + \omega_n^2} \tag{3.2}$$

In the case of this analysis, the inputs to the system were taken to be the value of the PPM signals sent by the communication module, and the outputs were taken to be the change in position of the quadcopter for the respective degree of freedom. While the actual dynamics of the quadcopter are certainly more complicated and interrelated, this model was determined to be sufficient to design a preliminary control algorithm.

To experimentally estimate ω_n and ζ, the quadcopter was subjected to a variety of step tests. These tests were carried out for each degree of freedom,

and were conducted by instantaneously changing the setpoint by one unit, in this case, 1 inch. Immediately before the step input was applied, the control for the degree of freedom being analyzed was changed to purely proportional control (i.e. $K_i = K_d = 0$), with the value of K_p selected such that the once the step input was applied the position of the quadcopter would oscillate about the new setpoint. The gains for the remaining degrees of freedom were selected so that they would provide the minimum amount of control necessary to keep the quadcopter hovering in view of the camera so as to avoid interfering as much as possible. The frequency and the growth/decay of those oscillations could then be used to estimate the transfer function of the system, which has the form

$$G(s) = \frac{K_p \omega_n^2}{s^2 + 2\zeta\omega_n s + (1 + K_p)\omega_n^2} \tag{3.3}$$

where ω_n and ζ refer to those of the *proportionally controlled system* and not those of the quadcopter itself. However, these quantities can be used to calculate those of the quadcopter directly by the following relations [23]:

$$\omega_{n,system} = \omega_{n,copter}\sqrt{1 + K_p} \tag{3.4}$$

$$\zeta_{system} = \frac{\zeta_{copter}}{1 + K_p} \tag{3.5}$$

For each degree of freedom, these tests were performed several times with different values of K_p in order to validate these estimates. Examples of this estimation process and comparisons between the behavior of the quadcopter and the behavior predicted by the model are shown in Figure 3.6.

During the course of these tests it was determined that frequent changes applied to the rudder had the effect of destabilizing the flight of the quadcopter. As a result, a much simpler method to control the yaw angle was used that did

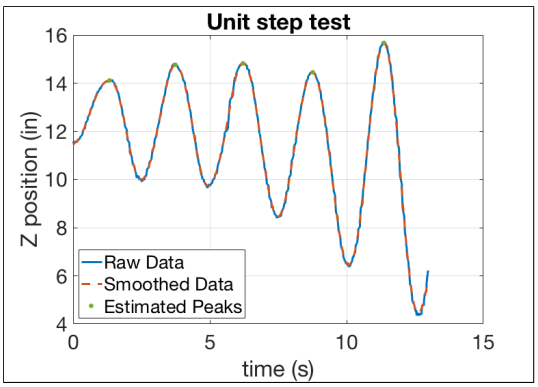

(a) Estimation of natural frequency

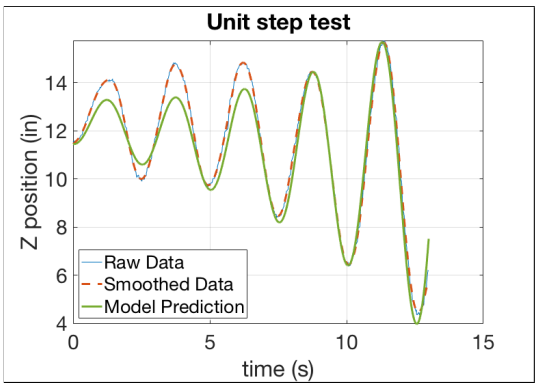

(b) Estimation of damping ratio and model prediction

Figure 3.6: Results from unit step test in Z-direction. The quadcopter is unstable under proportional control regardless of the value of K_p, indicating a negative value for ζ.

Table 3.3: Estimates of natural frequency and damping ratio from unit step tests such as the one shown in Figure 3.6. These estimates were made using multiple quadcopters with multiple values of K_p.

Degree of Freedom	ω_n (rad/s)	ζ
Z	0.7 (0.11Hz)	-0.15
X,Y	0.43 (0.07Hz)	-0.75

not require frequent changes to the rudder command: if the yaw angle exceeded a set threshold, a constant signal was sent to rotate the quadcopter until it returned to within a certain tolerance of the setpoint. The threshold, signal value, and tolerance were determined through trial and error.

The estimates of ω_n and ζ for the remaining degrees of freedom can be seen in Table 3.3. Having obtained these models, it was then possible to use Matlab's PID Tuning tool to design and optimize the PID controllers for each degree of freedom of the quadcopter. Note that the damping ratios are negative, indicating that control is needed to keep disturbances from growing in an unbounded manner.

To give the quadcopter the best chance of flying successfully in turbulence, the response time of the controller was brought as close as possible to a characteristic time scale of the turbulence. The parameter used to characterize the response time of the quadcopter was rise time t_R, or the amount of time taken to move from 10 to 90 percent from low value to high value when subjected to a step test [23]. The characteristic time scale of the turbulence was taken to be the eddy interception time based on the integral length scale, or

$$T_e = \frac{L}{U} \tag{3.6}$$

For a turbulent flow with a mean flow velocity of $1m/s$ and a correlation length of $10cm$, which is representative of the experimental conditions, the eddy interception time would be

$$T_e = \frac{0.1m}{1m/s} = 0.1s \tag{3.7}$$

Due to limitations of the hardware and the simplifications made by the model, not every tuning suggested by the software actually resulted in stable flight. As a result, some trial and error was still needed even when using the software tools. Given the limitations of the model and of the hardware itself, the fastest achievable rise time while maintaining stable flight was the same for all controlled degrees of freedom, and was $\approx 0.25s$. Once the control algorithm was tuned, it was tested in a quiescent flow, a laminar flow in the wind tunnel, and, having succeeded in both scenarios, was flown in a flow as fast and turbulent as possible. Having succeeded in flying in a turbulent flow with $U \approx 3.5m/s$ and a turbulence intensity of $\approx 17\%$, the control algorithm was deemed ready for experimental trials. The same PID gains were used for all quadcopters for all trials, and are reported in Table 3.4.

Table 3.4: PID gains from transfer function approximation. These gains were used for all quadcopters for all trials. A separate, empirically determined control scheme was used for takeoff.

Degree of Freedom	K_p	K_i	K_d
Z	10.3	2.90	9.14
X,Y	40.8	13.06	31.87

3.5 Motion Tracking System

The effectiveness of the quadcopter control system was dependent on accurate and timely measurements of the quadcopter's position. To this end, an optical motion tracking system was designed and implemented.

3.5.1 Image Capture

The quantity of interest used to estimate the rate of image capture necessary was the inverse of the eddy interception time, or

$$f_e \approx U/L \tag{3.8}$$

The rate of image capture needed to measure accurately on this time scale is the Nyquist frequency, or double this frequency. Using an initial estimate of a mean flow velocity of $5m/s$ and an integral length scale of $10cm$, an estimate of

$$f_s = 2 \times \frac{5m/s}{0.1m} = 100fps \tag{3.9}$$

was used. The implication of this estimate was that, in order for the whole system to run in real time, all image capture, image processing, and quadcopter control operations would have to take place in the span of $10ms$. In order to meet this requirement, careful considerations had to be made with regards to

image type and resolution so that the image processing burden could be as low as possible while maintaining adequate precision.

The camera selected was the Mightex SME-B012-U, which has fully adjustable resolution and frame rate and captures black and white images. Because of data transfer rate limitations from the camera itself, the maximum resolution at 100fps was 640×480 pixels, which was judged to allow sufficient precision given the predicted range of quadcopter motions. This camera has the added feature of being compatible with an external trigger, allowing for multiple cameras to be synchronized. The camera was used in conjunction with an adjustable focal length wide-angle lens so that the whole width of the tunnel floor could be seen with the end of the lens flush with the tunnel ceiling.

The original plan was to use two of these cameras to determine the position of the quadcopter in three dimensions, with an external trigger signal being used to synchronize the image capture. The hardware and code necessary to implement this scheme were developed, but because of the limited ports of vision into the wind tunnel and the complexity of calibrating the conversion of image data into coordinates of physical space in real time, motion tracking was implemented using only one camera located directly above the quadcopter. This system will be explored in more detail below.

An unforeseen consideration for frame rate arose from the lighting scheme used to illuminate the interior of the wind tunnel, which was done using a single LED floodlight that was plugged into wall power. Because of the 60Hz oscillation of the A/C wall power, capturing images with an exposure time of less than the period of the wall power oscillation ($\approx 16.67ms$) resulted in oscillating light levels in successive images. To remedy this issue, the exposure time for

each image had to be increased to as close to the period of the wall power as possible. Along with latencies in the shutter and data transfer, the the added exposure time reduced the frame rate to approximately 53fps. While the frame rate was reduced, the wind speed used for experiments was reduced by a factor of almost five from the wind speed used in the initial estimate in equation (3.9). Given the increased time scale from the change in wind speed, the reduced frame rate remained sufficiently fast to capture the relevant time scales.

3.5.2 Image Processing

Once an image of the quadcopter in flight was captured by the camera, it was necessary to extract the position of the drone for each degree of freedom (X,Y,Z,yaw) to pass to the control algorithm. To extract the necessary data, an image processing algorithm was developed using C++ and OpenCV, an open source library of image processing functions. C++ was chosen because of its efficiency and its compatibility with image processing libraries and the camera's developer SDK.

The first step in the image processing algorithm was to eliminate the effects of image distortion which occur due to the optical design of lenses. These effects cause pixels throughout the image to correspond non-uniformly to physical space, and can introduce significant errors. Especially since a wide angle lens was used to obtain the necessary field of view inside the wind tunnel, the effects of image distortion, particularly towards the edges of the image, could not be ignored. To correct for the effects of distortion, a camera calibration process was performed.

This process corrects for two types of distortion: radial, which occurs when light rays bend more at the edge of the frame than the center, and tangential, which occurs when the image plane is not parallel to the lens [24]. To correct for radial distortion, an OpenCV algorithm uses the following relations to correct the position of a pixel originally at position (x, y):

$$x_{corrected} = x(1 + k_1 r^2 + k_2 r^4 + k_3 r^6) \tag{3.10}$$

$$y_{corrected} = y(1 + k_1 r^2 + k_2 r^4 + k_3 r^6) \tag{3.11}$$

where r is the distance of the pixel (in pixels) from the distortion center. To correct for tangential distortion, the following relations are applied:

$$x_{corrected} = x + [2p_1 xy + p_2(r^2 + 2x^2)] \tag{3.12}$$

$$y_{corrected} = y + [p_1(r^2 + 2y^2) + 2p_2 xy] \tag{3.13}$$

The coefficients k_1, k_2, k_3, p_1, and p_2, are called the distortion coefficients. Two additional parameters are needed, the camera's focal length (f_x, f_y) and optical center (c_x, c_y). These two parameters are used to form a camera matrix, which can be used remove distortion for a camera independent from individual lenses. This matrix has the form

$$camera\ matrix = \begin{bmatrix} f_x & 0 & c_x \\ 0 & f_y & c_y \\ 0 & 0 & 1 \end{bmatrix}$$

The distortion coefficients and camera matrix are calculated using a set of images of a black and white chessboard pattern (Figure 3.7) in various locations of the camera's field of view. This calibration process only has to be performed once for a given camera setup, and once the coefficients are calculated they can

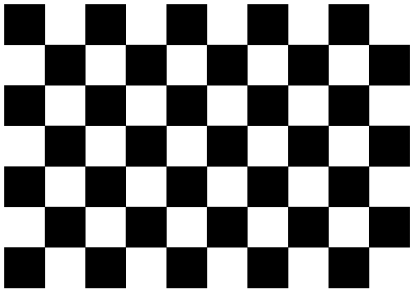

Figure 3.7: Chessboard pattern used for camera distortion calibration. This pattern was printed to fill an 8.5×11" sheet of paper. [24]

be saved and used to quickly "re-map" the positions of the pixels of all images taken by the camera, ensuring a uniform mapping of pixel space to physical space [24].

The second step of the image processing algorithm was to reduce the effects of noise by blurring the image. A simple Gaussian blur was applied, with the kernel size being determined using trial and error in conjunction with the steps that follow.

With the image sufficiently free of distortion and noise, the position of the drone could be extracted. Since the camera captured gray-scale images, a scheme was developed that used contrast between light and dark. To promote contrast, as much of the quadcopter as possible was painted white, white propellers were used, and the background was covered with a white material. Two black dots were affixed to the quadcopter for the algorithm to track, with one at the center of the top of the body and one behind the quadcopter affixed to the blade guard. The placement of these dots can be seen in Figure 3.8.

To determine the location of these dots using image data, two methods were tried and were compared using criteria of accuracy, defined using the error of

Figure 3.8: Quadcopter configuration for motion tracking system. The quadcopter has been painted white to promote contrast with the black dots, which are used by the motion tracking system to determine the location of the quadcopter. The white plastic frame protects the propellers in the (likely) event of a crash.

the method relative to both actual position and repeated measurements; robustness, defined by how often the method failed to return the position of a dot; and how long the process took to run. The first method applied used contour detection, which finds the edges of the dots and uses them to fit circles and calculate their centers. The second method used "blob" detection, which finds contiguous regions of pixels based on a variety of criteria (e.g. pixel value, circularity, convexity, minimum area). The contour-finding method proved to be the most accurate and the fastest, and acceptably robust for a stationary or slowly moving quadcopter. However, during flight, with the propellers spinning and the quadcopter moving rapidly, this method had issues consistently finding dots. Therefore, the blob detection method was pursued.

When using the blob detection method, every additional criterion used adds to computation time. The key way of reducing the number of criteria needed was carefully setting up the field of view. By ensuring that there was a large

degree of contrast between the black dots and the light quadcopter and background, accurate and robust dot detection was possible using thresholding based on pixel value alone. To do this, a binary image was created from the original image. In an 8-bit gray-scale image, all pixels have an integer value between 0 and 255, with 0 corresponding to black and 255 corresponding to white. In a binary image, all pixels have a value of exactly either 0 or 255. With an appropriate threshold applied to the original image, the new binary image consists only of black dots against a white background, making the blob detection quick and easy. Once the positions of the centers of the two blobs were found, the vector between the dots was calculated. A visualization for the steps of the image processing algorithm can be seen in Figure 3.9.

In order to determine the actual position of the quadcopter in physical space, the measurements had to be converted from pixel space. A non-constant correlation was needed, since as the position of the quadcopter changes vertically, the relation of pixel space to physical space changes. To make this conversion, the magnitude of the vector between the dots was used to determine the distance of the quadcopter from the camera. Because the dots are a fixed physical distance apart, they would appear to be closer together the farther the quadcopter moved away from the camera. For each individual quadcopter used, an experimental relation was determined between the distance of the quadcopter from the camera and the magnitude in pixels of the vector between the two dots. An additional empirical relation was determined between the distance of the image plane from the camera and the pixel density (i.e. pixels per unit distance). This relation was determined by calculating the average magnitude of the vectors between nine dots equal distance apart at known distances from the camera. Sample calibration curves can be seen in Figure 3.10.

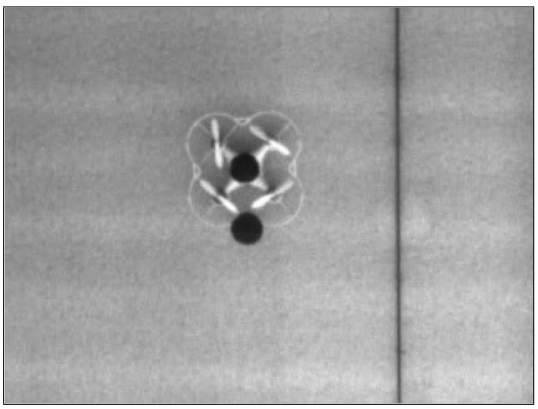

(a) Original image

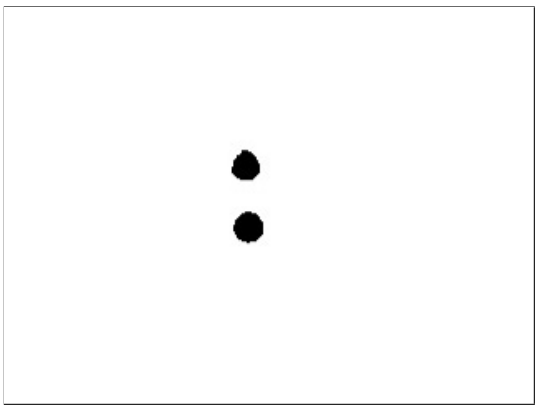

(b) Binary image

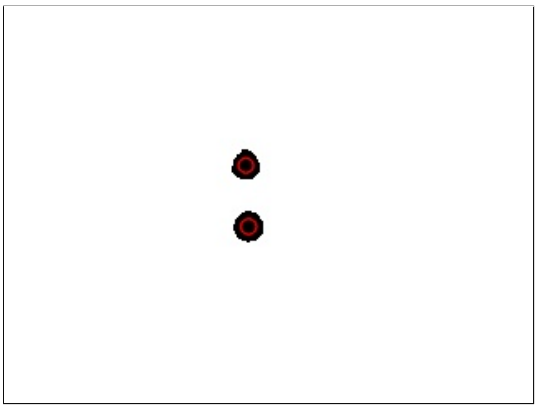

(c) Detected blobs

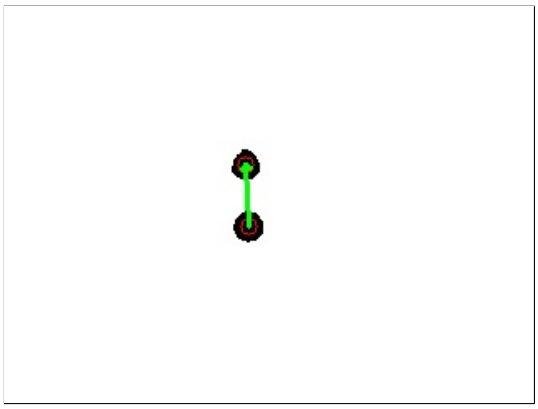

(d) Vector between blobs

Figure 3.9: Image Processing steps. First, the original image is corrected for distortion. A Gaussian blur is applied to remove noise, and then the image is thresholded to create a binary image. The blob detection algorithm finds the centers of the two dots and calculates the vector connecting them. The angle and magnitude of this vector in conjunction with the location of the centroid of the dot at the quadcopter's center are used to calculate 3D position.

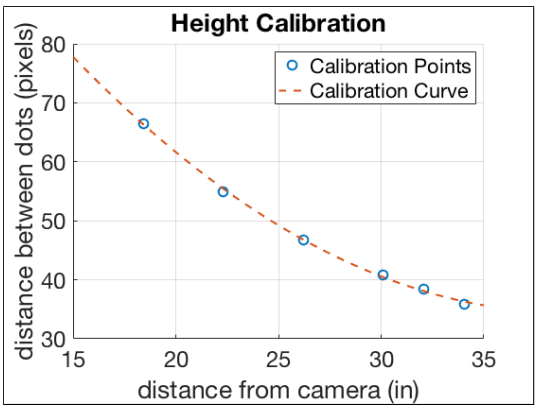

(a) Vertical (Z) position calibration

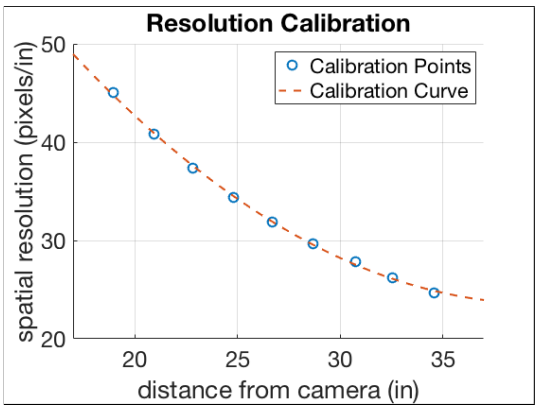

(b) Spatial resolution calibration

Figure 3.10: Sample curves for image processing spatial calibration. These two relations used in conjunction allow for direct conversion of measurements from pixel space to physical space using a single image. (b) is used for all quadcopters, while (a) must be determined for each individual one.

At this point, no more information was needed to determine the position of the quadcopter relative to each of the four degrees of freedom. The yaw angle was independent of vertical position and was simply the angle of the vector between the two dots, Z position was calculated directly from the magnitude of the vector between the two dots, and X and Y position were calculated by dividing their position in pixels by the spatial pixel density at the corresponding Z position.

3.6 Turbulence Generation and Measurement

This project was carried out using a low speed, low background turbulence wind tunnel which has many features that made it desirable for use in this investigation. The ability to run at low speeds with low background turbulence was of particular importance, since it allowed for confidence that the only

turbulence in the tunnel was turbulence that had been intentionally generated. The test section has a square cross section of $91 \times 91 cm^2$ and a length of $9.1m$. This large cross-section area maintained a large homogeneous core of the flow through the end of the tunnel despite the growth of the boundary layer [25], meaning that flight testing was possible at any desired location within the tunnel. As discussed below, since the properties of turbulence generated by grids evolve as the flow moves downstream, the long test section allowed for a wider range of turbulent conditions to be utilized than would have been possible for wind tunnels with shorter test sections. The diagram for the wind tunnel is shown in Figure 3.11, and photographs are shown in Figure 3.14.

In order to run produce a stable low wind speed free from oscillation as desired for this experiment, a small modification was made to the tunnel. A plywood board was used to cover a portion of the wind tunnel's fan exhaust, which by decreasing its area decreased the mean wind speed for a given fan speed. The uniformity of the flow and the homogeneity of the turbulence for this configuration was verified using hot wire measurements as discussed below. A picture is shown in Figure 3.15.

3.6.1 Turbulence Generation

To provide as many data points as possible for testing the susceptibility model laid out, turbulent flows with a variety of intensities and integral length scales were desired. In terms of turbulence intensity, both very low and very high cases were desired. Given the capabilities of the wind tunnel, low turbulence cases ($< 1\%$) were easy to generate. The upper bound on turbulence intensity

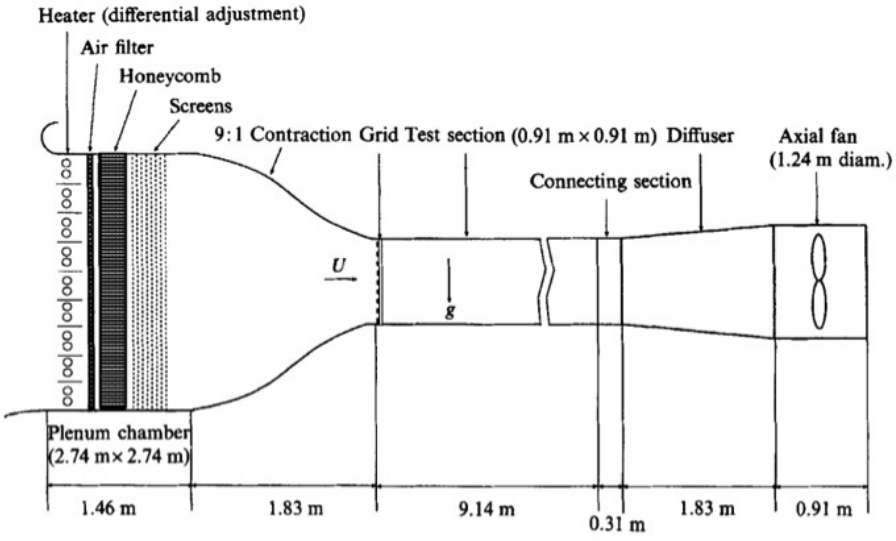

Figure 3.11: Sketch of wind tunnel [25]. This suction-driven wind tunnel was specifically designed to generate flows with low background turbulence at low speeds with a large homogeneous core throughout the entirety of the test section.

was the maximum that could be generated using the techniques available in the laboratory.

To create the desired experimental conditions, turbulence in the wind tunnel was generated using several different grids. Two of these grids were classical grids composed of evenly spaced bars, and one was an active grid, which is composed spinning vanes powered by servo motors. The characteristics of the turbulence generated by these types of grids have been well studied and were selected to produce homogeneous turbulence as desired for this experiment [2] [26]. An example of each type of grid used in this experiment can be seen in Figure 3.12.

Each grid produces turbulence with different intensities and integral length scales, which are quantified in section 3.6.2. The properties of the flow evolve relative to the distance away from the grid, so by changing grids as well as po-

(a) Classical Grid (1″ Spacing)

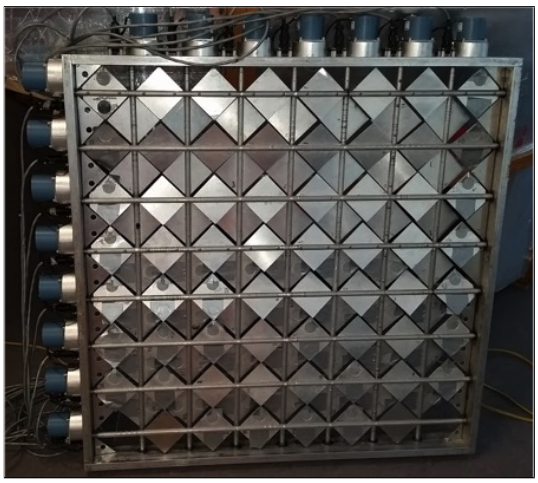

(b) Active Grid

Figure 3.12: Turbulence Generation Grids. When placed at the beginning of the test section as shown in Figure 3.11, they create homogeneous turbulence with different intensities and integral length scales. An additional classical grid with 4.5″ spacing was used but is not pictured here. The active grid generates the most intense turbulence and the longest length scales.

sition within the tunnel, a range of turbulence conditions could be generated [2] [26]. Turbulence intensities higher than the highest value reported here were generated by fixing alternating vanes of the active grid in place, but this configuration was discarded since it was found to not produce uniform flow profiles.

3.6.2 Turbulence Measurement

The mean speeds, turbulence intensities, and integral length scales of the different flows in this experiment were determined by measurements obtained using constant temperature hot wire anemometry. Measurements were taken when quadcopters were not flying in the tunnel.

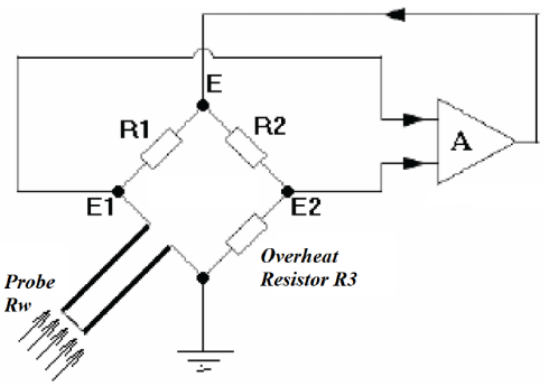

Figure 3.13: Circuit diagram for constant temperature hot wire anemometer. The resistance *Rw* is temperature dependent and changes with the velocity of the flow passing over it. The voltage difference between E1 and E2 is used by the feedback circuit A to send a current to maintain a constant temperature of the wire. Voltage E is used to directly calculate flow velocity [27].

A circuit diagram for a constant temperature hot wire anemometer can be seen in Figure 3.13. The probe itself is composed of a thin cylindrical wire strung between two prongs, and the anemometer circuit is composed of a Wheatstone bridge and an operational amplifier. By setting the resistance of the Overheat Resistor (R3) and running a current through the circuit, the temperature of the wire is raised above room temperature. As flow passes over the wire, the temperature of the wire drops. Since the resistance of the wire is a function of its temperature, there is a corresponding change in the voltage between E1 and E2. The feedback portion of the circuit uses this voltage difference to determine a correction current to send to keep the wire at a constant temperature, and the voltage E can be directly related to flow velocity using an empirical relation called King's Law [28].

The measurements for the grid/tunnel position configurations used in the experiment can be seen in Table 3.5. Two testing stations were used, corresponding to the locations in the tunnel where the quadcopters were flown: Window 6, which was located $3m$ downstream from the grid, and Window 14, which

Table 3.5: Hotwire Measurements for different grids shown in order of increasing turbulence intensity. U was maintained at a constant value of $1.15m/s$. These measurements were taken separately from quadcopter flight trials.

Grid	Window	$u'/U(\%)$	L (in/cm)
1″	14	0.75	1.85 (4.7)
	6	1.31	1.3 (3.3)
4.5″	14	1.85	2.28 (5.8)
	6	3.25	1.81 (4.6)
Active	14	7.05	3.46 (8.8)
	6	13.15	3.26 (8.3)

was located $7m$ downstream from the grid. The locations of these windows are shown in Figure 3.14. For a given grid, turbulence intensity decreases in the downstream direction, while the integral length scale increases. Window 14 was chosen to allow the integral length scale to grow as much possible since it was the farthest window downstream, and Window 6 was chosen to provide maximum turbulence intensity since it was positioned farthest upstream.

The mean speed was chosen due to practical limitations of the quadcopters. The maximum speed the quadcopters were able to successfully fly in the wind tunnel was around $3.75m/s$, but they had to accelerate gradually to that speed. Running the tunnel at a constant speed for all portions of a quadcopter's flight precluded the need to know the wind speed at any given point of time, so a mean wind speed that the quadcopters could take off into was preferred. By attempting takeoffs with the tunnel running at different speeds, a mean speed of $1.15m/s$ was chosen.

Table 3.6: Time scales for components of system architecture. The camera was found to capture images at a regular interval, and the image processing and communication took place in a consistent amount of time. The only variability in timing arose from the operating system task scheduler.

Component	Δt (ms)
Image capture interval	18.9
Image processing	4.6
Quadcopter communication	1.9

3.7 Time Scales

To ensure that the system would run consistently in the time frame needed, the relevant portions of the system were tested individually. Testing the timing of the camera was straightforward, since it recorded a time stamp as part of the image data. The image processing algorithm was timed using the computer's internal clock. The response time of the microcontroller/quadcopter communication was tested using a simple program that switched between two commands in decreasing intervals until the quadcopter stopped responding to the commands. The results from these tests are reported in Table 3.6.

An important note in regards to these results is that the software needed to run the camera could only run on the Windows 7 operating system. Windows 7 is not a real-time operating system, meaning that the timing for the execution of functions was subject to a variable buffer delay. As such, provisions had to be made to handle the fact that different portions of the system ran in the same amount of time but at varying intervals. One such provision was that the time associated with quadcopter position data was determined using image time stamps instead of the computer's internal clock. Additionally, a safeguard had to be implemented when sending commands to the quadcopter to ensure

that commands would not be sent in too quick of succession and overload the connection.

The time scale of the turbulence was taken to be the eddy interception time as defined in equation (2.8). The maximum value for this quantity was for the case of the active grid at Window 14, of

$$T_e = \frac{8.8cm}{1.15m/s} = 0.08s \tag{3.14}$$

The minimum value was for the case of the 1" passive grid at Window 6, with a value of

$$T_e = \frac{3.3cm}{1.15m/s} = 0.03s \tag{3.15}$$

3.8 Final Layout

The layout for all components described in the system architecture can be seen in Figure 3.14.

(a) Wind tunnel (side view)

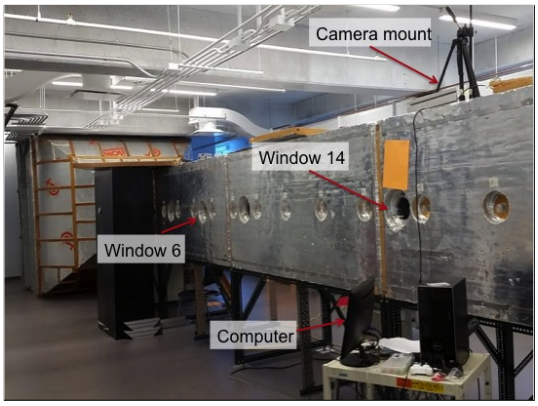

(b) Wind Tunnel (other side).

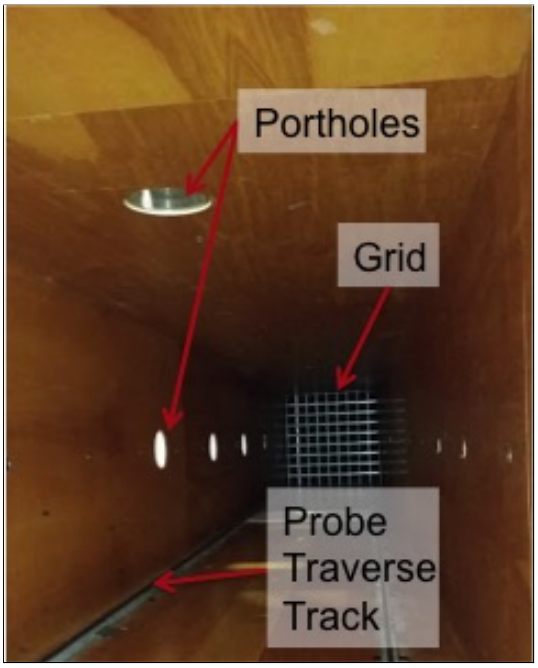

(c) Inside of the wind tunnel.

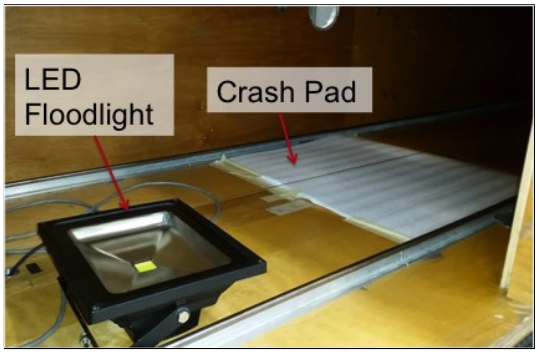

(d) Crash pad and LED floodlight

Figure 3.14: Final Layout. The wind speed inside the tunnel was controlled by changing the speed of the suction fan. The computer along with the communication module was placed on a cart that could be wheeled between the testing stations at Window 6 and Window 14. A camera was mounted at each station, and looked straight down into the tunnel through a porthole, with the end of the lens flush with the inner wall of the tunnel. Quadcopters were placed inside and removed from the tunnel through the portholes. To soften the landings of the quadcopters, a white foam "crash pad" was used. The LED floodlight is shown, and is oriented to provide even light with no shadows in the test area.

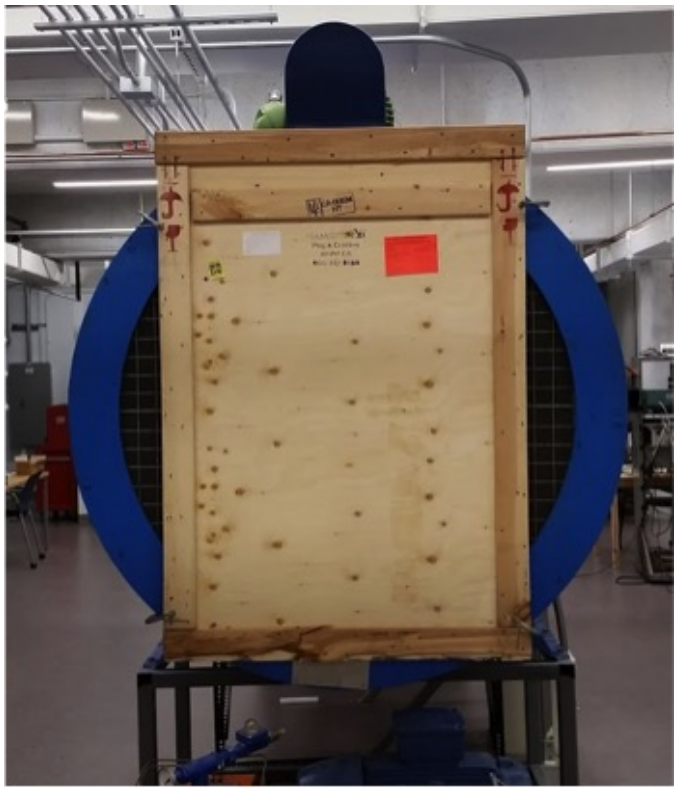

Figure 3.15: Plywood board used to modify the wind tunnel's exhaust area. This modification allowed for testing at stable low wind speeds.

CHAPTER 4

RESULTS

With the control algorithm and turbulence generation in place, the fleet of quadcopters was ready for flight in the wind tunnel. The degrees of freedom of the quadcopter relative to the wind tunnel are shown in Figure 4.1, with Y into the wind, Z vertical, and X horizontal perpendicular to the wind.

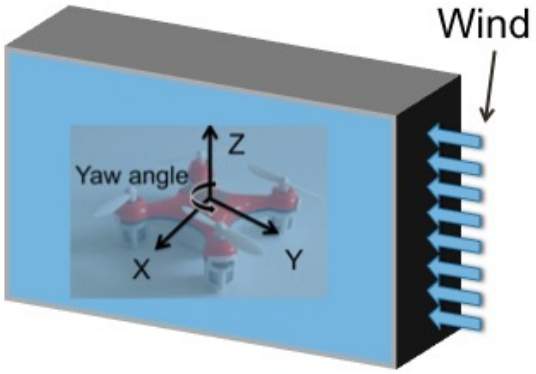

Figure 4.1: Quadcopter Axis Orientation. The quadcopter axes were oriented so that Y points into the wind, Z points up vertically, and X is horizontal perpendicular to the flow.

For each turbulence case, each quadcopter was flown for a total of approximately 10 to 15 minutes. Given the limitations of the battery life of the quadcopters, multiple flights for a given case were conducted with each quadcopter to reach this amount of flight time. To allow for comparison of statistics across multiple flights with the same quadcopter, the data for individual flights were combined for each turbulence case. For each individual flight, the portion of the flight data corresponding to the takeoff and crash landing were removed so that only the ”steady-state” portions of flight were considered, and the mean of each measured quantity was subtracted out to prevent artificial skewing.

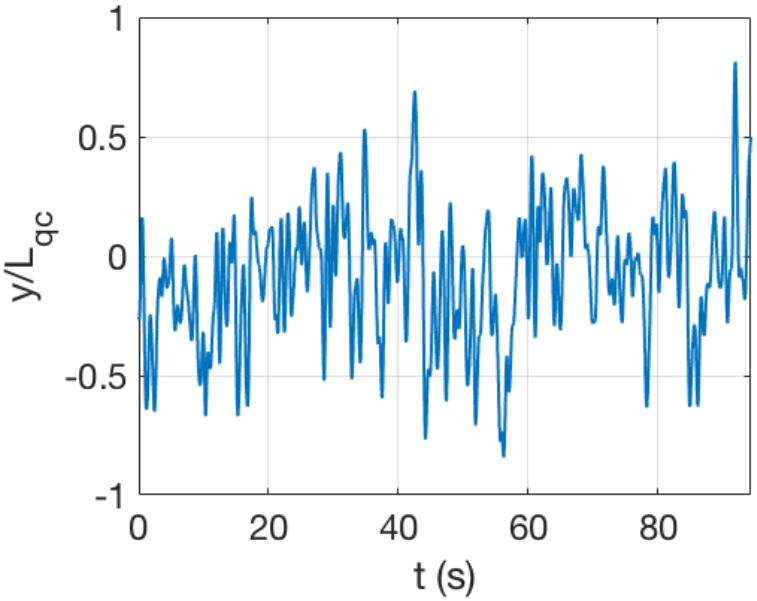

Figure 4.2: Sample trajectory for the quadcopter called Puffin. Position is relative to the setpoint, and is normalized by quadcopter length L_{qc}. Like the turbulent velocity signal shown in Figure 2.1, the signal appears to be chaotic but correlated with respect to time.

Surprisingly, fewer individual flights were needed to reach the desired duration of flight time for the higher turbulence cases than low turbulence cases. A sample trajectory for a single quadcopter is shown in Figure 4.2. The initial results for all quadcopters are shown in Figure 4.3, with displacements normalized by the length of the quadcopter, L_{qc}.

From these initial results, an important caveat arises with respect to equation (2.15): the data do not appear to intersect 0 displacement. The quadcopters each appear to have a baseline instability which needs to be accounted for. An adjustment is thereby made:

$$\frac{\left\langle x^2 \right\rangle^{1/2}}{L^*} = C\left(\frac{\rho A L^*}{m}\right)\left(\frac{u'}{U}\right)^2 + b \tag{4.1}$$

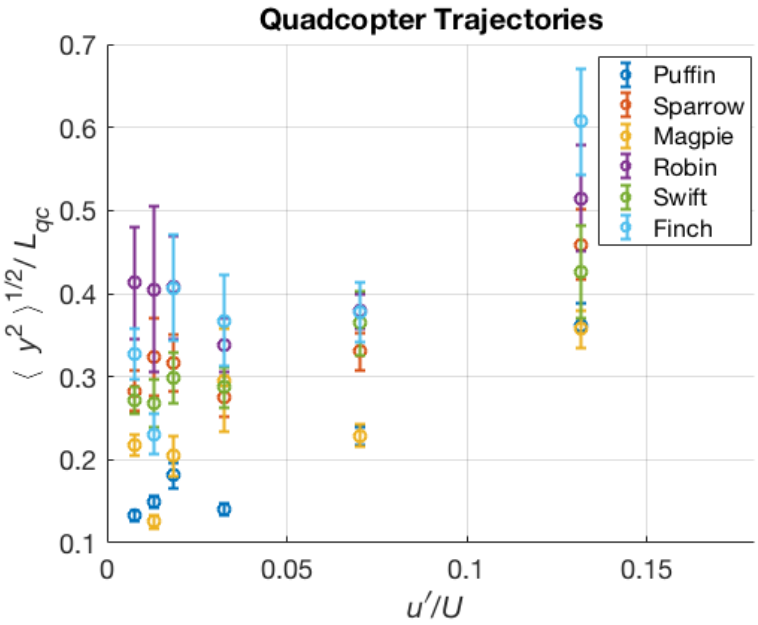

Figure 4.3: Quadcopter displacement normalized by quadcopter length L_{qc}. The displacements appear to vary as turbulence intensity squared. However, the data do not appear to intersect 0 displacement, requiring the addition of an offset term to equation (2.12). Error bars represent standard error.

with b representing a base instability for a given quadcopter. A more rigorous definition for b is a subject for future investigation. An initial attempt to benchmark this instability was done by flying the quadcopters in a quiescent flow, but the displacements were larger than for the low turbulence cases across quadcopters and axes. This occurrence was likely due to interactions of the quadcopter with its own wake while flying in quiescent flow, the effects of which were mitigated when the flow swept the quadcopters' wake downstream. While a quadratic relation with turbulence intensity as earlier proposed seems plausible, turbulence intensity was not the only variable changing across trials.

With the model thus adjusted, the next step was the determination of the relevant length scale L^*. A first guess regarding this length scale was the integral length scale. However, the experimental tools used in this investigation did not allow for turbulence intensity and integral length scale to be varied indepen-

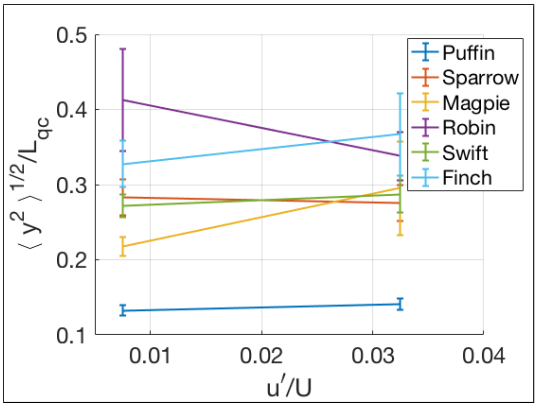

(a) Comparing left to right: $L = 1.85in$ and $L = 1.81in$.

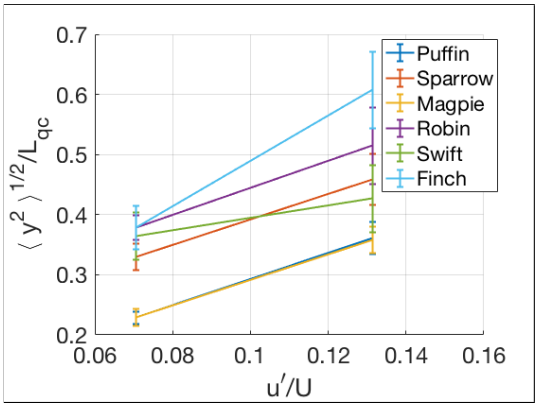

(b) Comparing left to right: $L = 3.46in$ and $L = 3.26in$

Figure 4.4: Comparing cases of similar integral length scales. While more clear in (b), all that can be shown is that displacement increases with turbulence intensity when L is approximately constant. Further investigation is needed to determine effects of changing L.

dently while maintaining the same mean wind speed. As such, there were only two sets of two cases where the integral length scales were approximately the same, the comparisons for which are shown in Figure 4.4. From only these two sets of cases, it is difficult to make a definitive claim regarding the role of the integral length scale.

In the absence of data to determine the relevance of the integral length scale, another method was needed to make an estimate of the length scale L^* from equation (4.1). Just as correlation functions and kinetic energy spectra can be used to provide information regarding energetic length scales in turbulence, these techniques were applied to the trajectories and velocities of the quadcopters to provide insight in estimating the relevant length scale. Velocities were calculated by fitting second order polynomials to position data, with the number of points chosen such that the kurtosis of velocity converged. A more

detailed explanation of velocity and acceleration estimates can be seen in the Appendix.

The first step was to examine the autocorrelation functions of position and velocity, which can be seen in Figure 4.5. Correlation times were estimated by fitting a curve of form

$$e^{-t/\tau} \tag{4.2}$$

to the autocorrelation functions, with τ used as the estimate for correlation time. Across turbulence cases, and across different axes, the correlation times for position were found to vary significantly, ranging from $0.5s$ to $3.5s$. However, across all turbulence cases and axes, the correlation times for velocity were found to be the same within $0.05s$, which would seem to indicate a time scale independent of turbulence intensity or integral length scale. To validate this observation, a comparison was made between the turbulent kinetic energy spectra and the power spectral densities of quadcopter velocities. One such comparison is shown in Figure 4.6, along with the frequency corresponding to the frequency of the integral length scale for the higher turbulence case. A $-5/3$ power law, which is the slope of the inertial subrange for a turbulent flow, is shown for comparison [2].

The most pronounced difference in the shape of the quadcopter velocity spectra appeared to occur at a time scale slower than that of integral length scale. Additionally, both quadcopter velocity spectra appeared to have a spike at a frequency of approximately 1Hz. As shown in Figure 4.7, comparing quadcopter velocity spectra across different turbulence cases showed that this peak increased in value but remained at the same frequency as the turbulence intensity increased.

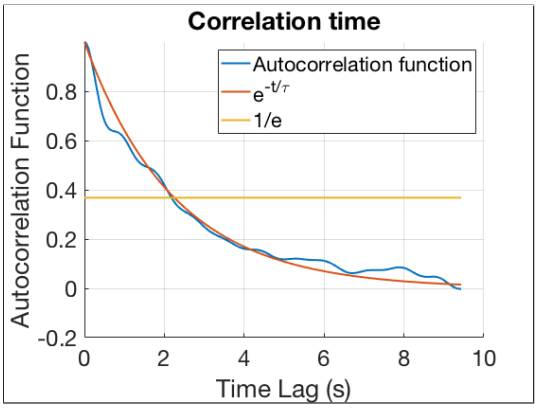

(a) Autocorrelation function vs. time for Y-position. $\tau = 2.25s$.

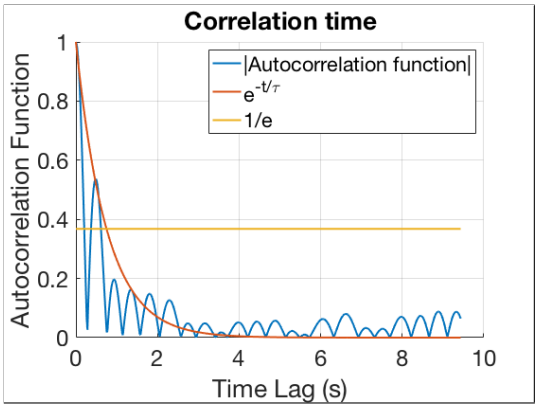

(b) Autocorrelation function vs. time for Y-velocity. $\tau = 0.75s$

Figure 4.5: Autocorrelation functions for Y-position and velocity. The absolute value of the ACF for velocity is shown because of its oscillatory nature. While the autocorrelation functions for position varied across turbulence cases and axes, those for velocity remained constant. This implied a velocity correlation time, and therefore relevant length scale, independent of the properties of the turbulence used in this investigation. Integrating under the velocity ACF until it reached a value of $1/e$ returned a correlation time within $0.05s$ of the rise time t_R of the quadcopter for all axes.

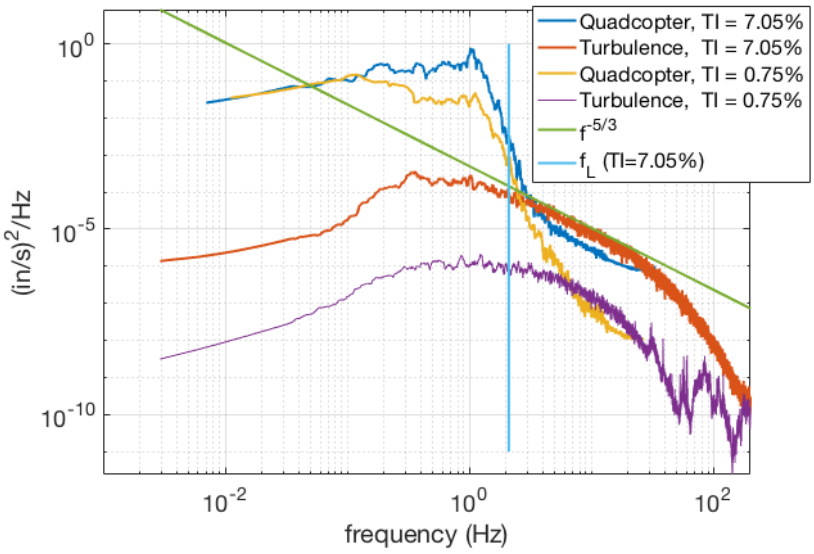

Figure 4.6: Turbulent Kinetic Energy (TKE) spectra compared with quadcopter power spectral density (PSD) for *Y*-velocity. The TKE spectra are scaled by the same factor to facilitate comparison with the quadcopter PSDs. The slopes of the quadcopter spectra appear similar to those of the turbulence at frequencies faster than that of the integral length scale, but the energy content in this region is several orders of magnitude lower than at lower frequencies. The region of interest regarding quadcopter spectra shapes is therefore at frequencies around and below 1Hz.

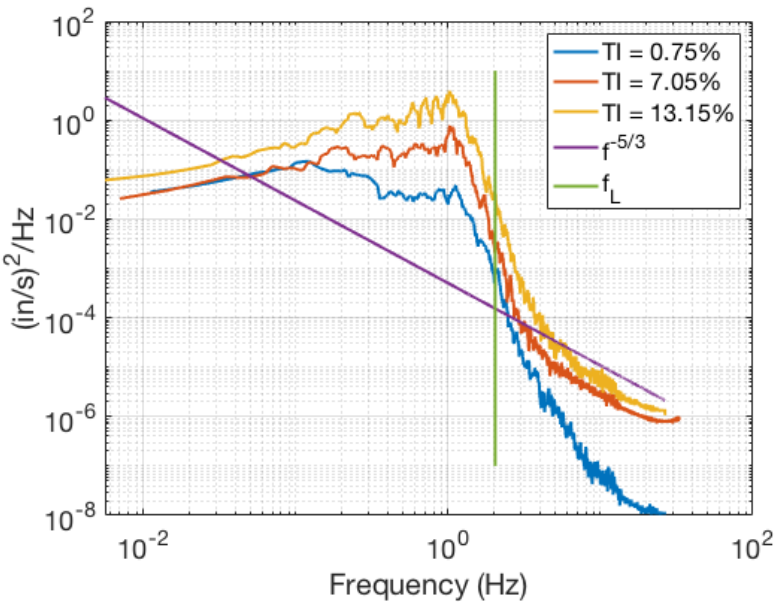

Figure 4.7: Power spectral density for Y velocity at different turbulence intensities to observe effects of changing turbulence intensity on the 1Hz peak initially found in Figure 4.6. The peak remained at the same frequency, implying that its location was due to a factor other than turbulence intensity or integral length scale.

With evidence implying a constant relevant time scale independent of turbulence intensity or integral length scale, the possibility was explored that the time scale of the response of the quadcopter to perturbations was more dominant than the time scale of the perturbations themselves. Due to the limitations of the quadcopter as discussed in section 3.7 and the maximum integral length scale able to be generated, the ratios of these time scales were a minimum of

$$\frac{t_R}{T_e} = \frac{0.25s}{0.08s} \approx 3.1 \tag{4.3}$$

where T_e is the eddy interception time as defined in equation (2.8). A rich area for possible exploration exists regarding what happens when this ratio is less than or equal to 1, as will be discussed in a later section.

As would be done in estimating a correlation length scale in turbulence, a correlation time scale for the quadcopters was estimated by integrating under the velocity autocorrelation function [2]. Since the autocorrelation function oscillated, the absolute value of this function was used. The cutoff value for the integration domain was taken to be where the autocorrelation function reached a value of $1/e$, which is a common choice when estimating the integral length scale [2]. Performing this calculation returned a correlation time of $0.30s$, which was within $0.05s$ of the estimated rise time t_R of the quadcopter. Therefore, using the rise time of the quadcopter as the relevant time scale, the relevant length scale for equation (4.1) was estimated as the length of the air column in the flow swept past the quadcopter during its rise time, or

$$L^* = t_R \times U \tag{4.4}$$

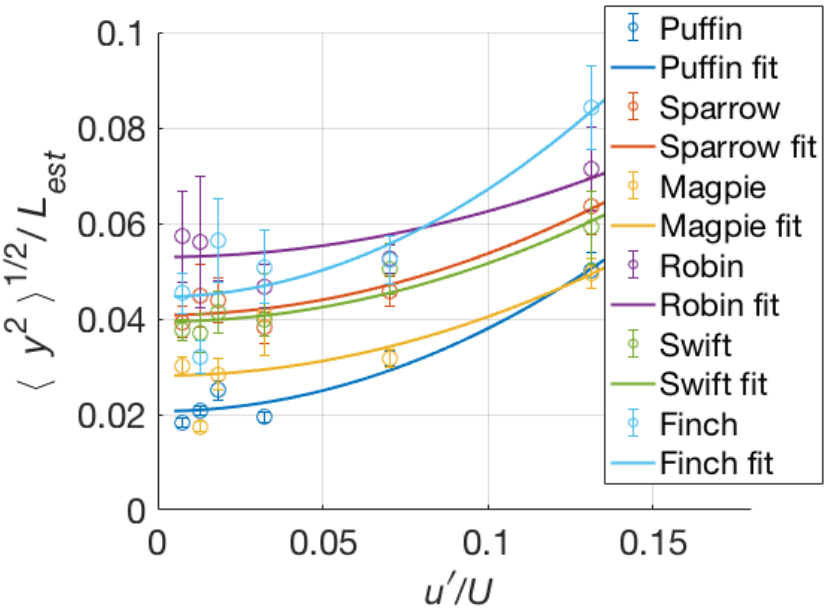

Figure 4.8: Quadcopter displacement normalized by estimated length scale for Y displacement. A curve of the form of equation (4.1) was fit to the data for each quadcopter. As in Figure 4.3, error bars represent standard error. The values for C are reported in Table 4.1.

With a flow mean speed in all cases of $1.15m/s$, and a rise time of $0.25s$, the estimated length scale becomes

$$L^* = L_{est} = 0.25s \times 1.15m/s = \mathbf{0.29m} \tag{4.5}$$

With this estimate for the relevant length scale, equation (4.1) could be applied to use the displacement results to estimate the susceptibility C (Figure 4.8, Table 4.1). The area of the quadcopter was taken to be the area of the rectangle projected by the edges of the airframe in the relevant direction (i.e. X, Y, Z). The actual area is difficult to measure, due to the curvature of the airframe and the fact that the propellers are spinning. For the X-axis, the coefficients for two of the quadcopters were negative, implying that their displacement due to turbulence decreased with turbulence intensity.

Table 4.1: Estimates for the susceptibility C for the displacement of the quadcopters within a 95% confidence interval. These coefficients were the largest for Y, the direction into the wind. The coefficients for Z were the most consistent across all quadcopters. The coefficients for X showed more variation, including the unexpected negative dependence on turbulence intensity for Puffin and Swift.

Quadcopter	C_X	C_Y	C_Z
Puffin	-0.11	67.2	17.1
Sparrow	21.1	50.0	13.8
Magpie	12.8	47.8	8.5
Robin	16.5	37.2	1.7
Swift	-4.5	47.3	14.7
Finch	14.4	87.4	10.3

A general expectation regarding the values of C for different quadcopters was that higher susceptibility in one direction would imply higher susceptibility in other directions as well. To test this expectation, the values of C were plotted against one another, as shown in Figure 4.9. From these comparisons, however, the correlation between the values of C across different axes remains unclear. Susceptibility in the Z-direction appeared to be loosely negatively correlated with that of X, but loosely positively correlated with that of Y. Meanwhile, the susceptibilities in the X and Y-directions do not appear to be correlated. More data is likely needed to determine the correlation of these coefficients, in addition to a more rigorous definition of the offset b in equation (4.1).

With the correlation of susceptibility across different axes unclear, the displacements for each quadcopter were averaged for each turbulence intensity to get an estimate of susceptibility that depended less on the differences among the individual quadcopters. These graphs are shown in Figures 4.10, 4.11, and 4.12.

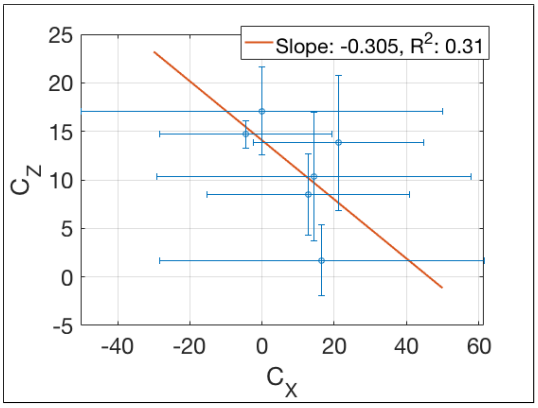

(a) Susceptibility C in Z-direction vs. in x-direction

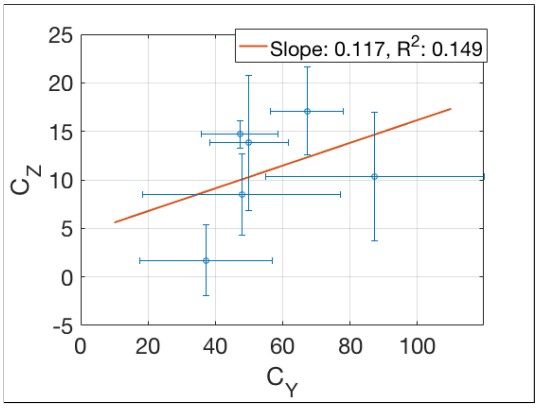

(b) Susceptibility C in Z-direction vs. in Y-direction

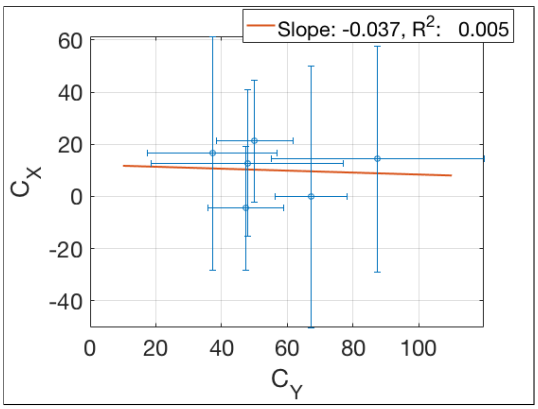

(c) Susceptibility C in X-direction vs. in Y-direction

Figure 4.9: Comparison of susceptibility C in different directions with least-squares linear fits. Because of the low R^2 values and variations in the signs of the slopes of the lines, a correlation between susceptibilities for different axes is unclear.

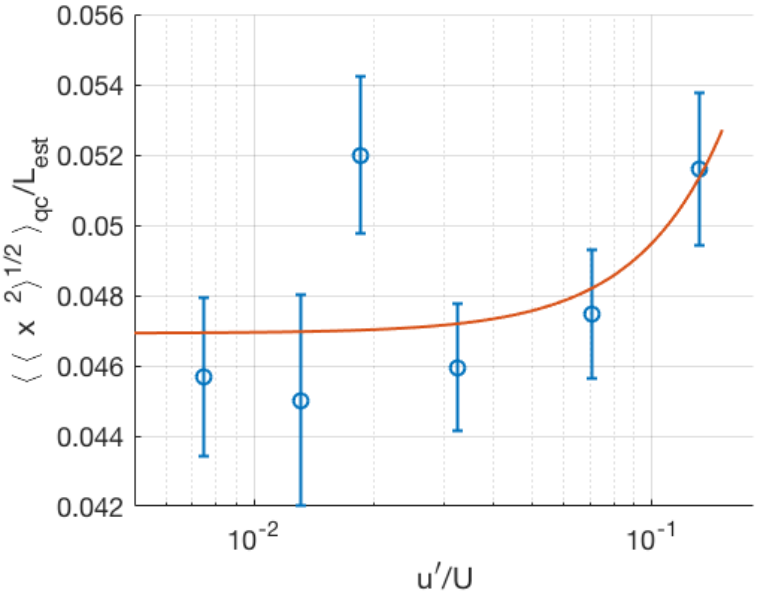

Figure 4.10: Displacement in X-direction averaged for all quadcopters. C = 10.0. The outlier was from the 4.5" passive grid at Window 6, the third data point from the left. This was the most difficult point to collect data at, since the flight times where uncharacteristically short for all quadcopters. The flights were as expected for the same grid at Window 14.

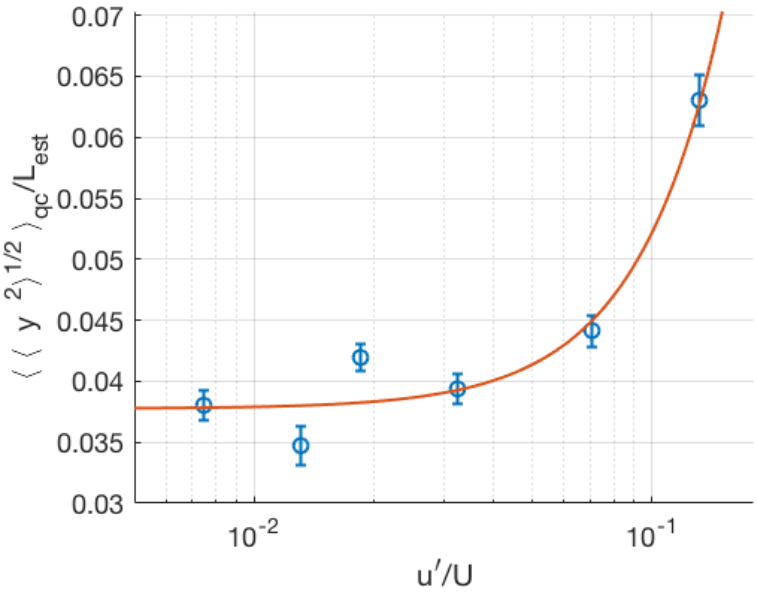

Figure 4.11: Displacement in Y-direction averaged for all quadcopters. C = 56.2.

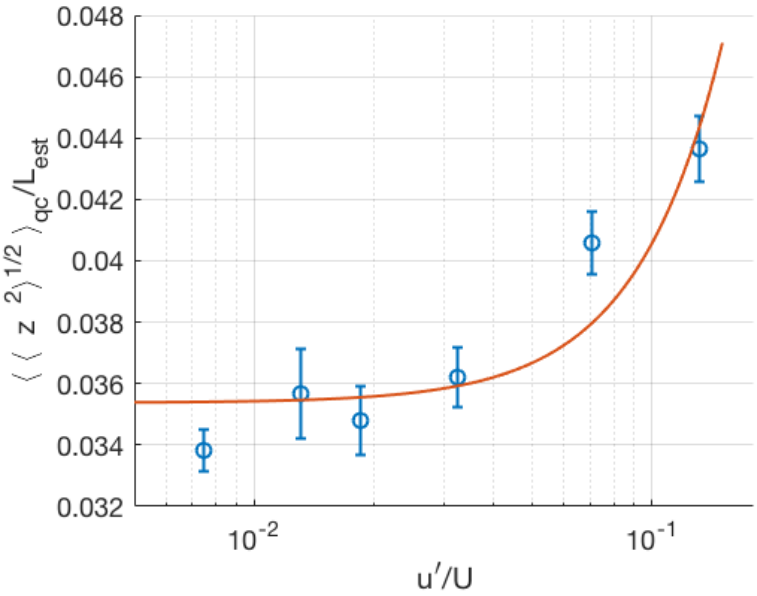

Figure 4.12: Displacement in Z-direction averaged for all quadcopters. $C = 11.1$.

To form a more comprehensive estimate of susceptibility, a total 3D displacement was calculated using the displacements for the X, Y, and Z-axes:

$$\langle \mathbf{x}^2 \rangle^{1/2} = \sqrt{\langle x^2 \rangle + \langle y^2 \rangle + \langle z^2 \rangle} \tag{4.6}$$

Using 3D displacement in equation 4.1, as shown in Figure 4.13, a susceptibility coefficient of $C = 19.4$ was predicted.

The case for which the total displacement least matches the trend, the 4.5″ grid at window 6 (third data point from the left), was the most difficult case to acquire data for, since for an undetermined reason the flight times for individual trials were uncharacteristically short before crashing for all quadcopters. The quadcopters flew as expected for the same grid at window 14.

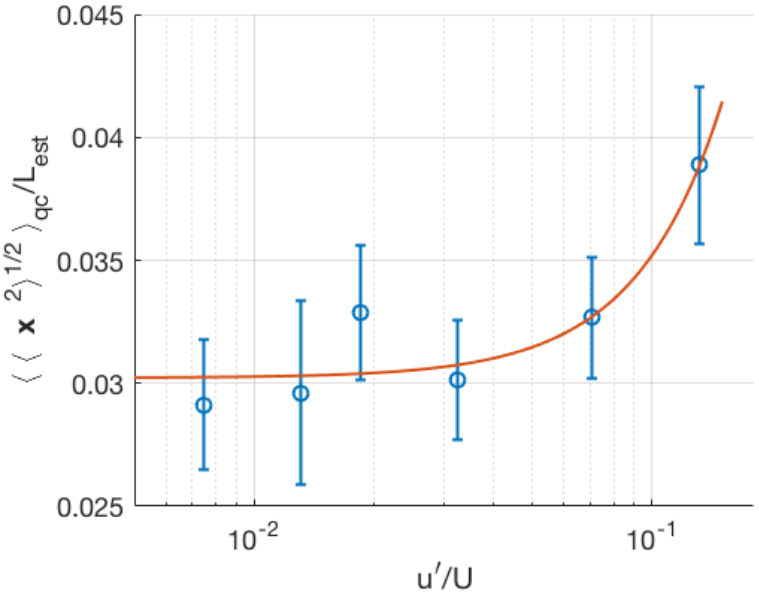

Figure 4.13: Total displacement vs. turbulence intensity averaged across all quadcopters. A susceptibility coefficient of 19.4 was predicted. Error bars represent standard error propagated across all quadcopters and directions.

CHAPTER 5

CONCLUSIONS

During the course of this project, an experiment was designed and conducted to determine the susceptibility of a small quadcopter to disturbances due to turbulence in a wind tunnel. A closed loop system was developed for flying quadcopters autonomously in order to conduct these experiments, which required designing an image processing and PID algorithm. A model for quantifying susceptibility statistically was developed and subsequently analyzed after flying the quadcopters in flows with a variety of turbulence intensities and integral length scales.

Experimental results corroborated the model of susceptibility developed during this project, laying the foundation for future investigations to better understand the effects of turbulence on quadcopters. This model provides a broadly applicable method for quantifying susceptibility to turbulence, allowing for different quadcopters and control schemes to be directly and concretely compared. By continuing this investigation, the susceptibility model can continue to be developed, and aid in the design of control schemes for more stable and efficient quadcopter flight in turbulence.

CHAPTER 6

FUTURE WORK

The results of this experiment demonstrate the plausibility of the susceptibility model laid out during this project, but open questions remain. The main open question pertains to identifying the relevant length scale, and answering this question requires determining the effects of the control algorithm response time and the turbulence integral length scale. The experiment as laid out can be used to investigate the effects of increasing the ratio of rise time to eddy interception time by slowing down the response time of the quadcopter, but additional work would need to be done to determine how to bring that ratio closer to or below 1. Additionally, a wider range of turbulence intensities should be explored than done thus far in this project to further strengthen the estimates of the susceptibility coefficients.

6.1 Control Algorithm Comparison

Now that a framework for a meaningful measurement of susceptibility has been developed, the relative performances of different control algorithms can now be compared. For PID controllers, the tunings can be altered to compare the behavior of the quadcopter with different ratios of rise time to eddy interception time. Other controller types such as Linear-Quadratic Regulator (LQR) or more predictive PID controllers with the addition of a feed-forward term can be developed and tested as well.

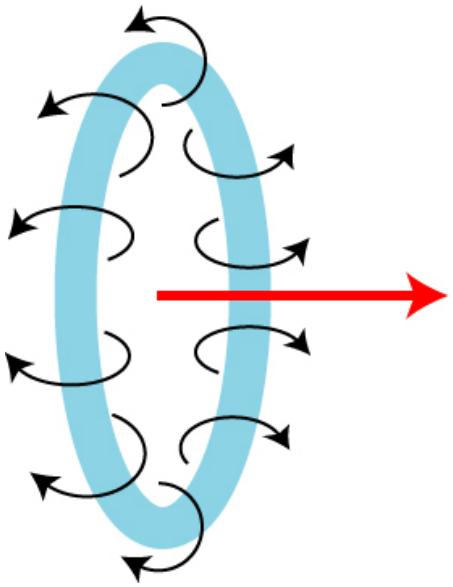

Figure 6.1: Vortex Ring [29]

6.2 Behavior of Quadcopter Disturbed by Vortex Rings

As discussed in section 3.7, there was a significant difference in scale between the eddy interception time based on the integral length scale and the response time of the quadcopter. A possible way to investigate the effects when these two time scales are the same would be to carry out a similar experiment with vortex rings instead of a homogeneous turbulent flow. A vortex ring, as shown in Figure 6.1, is straightforward to generate with specific velocity characteristics and dimensions. By placing the setpoint of the quadcopter at a specific location relative to the vortex ring, the direction of the velocity disturbance as well as the length scale of the disturbance would be known. As a result, much more specific information could be obtained regarding the nature of the disturbances to which the quadcopter was subjected. The results of such an experiment could be used in comparison with those from the one conducted here to estimate the length scale and time scales that affect the quadcopter in turbulence.

6.3 Quadcopter Modifications

While the quadcopters used in this project were suitable for acquiring the baseline results presented here, quadcopters with different characteristics would improve this investigation and allow it to move in other directions.

One limitation of the Cheerson CX-10 was its size. Despite its small size relative to most quadcopters, it remained very slow relative to the time scales of the turbulence. An even smaller and lighter quadcopter might be able to react more quickly to the flow and allow for the investigation of effects of length scales shorter than the integral length scale.

Another limitation was the manner in which the quadcopters had to be controlled. While the embedded orientation control was very helpful in getting this experiment off the ground both literally and figuratively, it added a layer of uncertainty with regards to how the quadcopter was actually responding to command signals. A quadcopter with a more flexible control scheme, or at least one that allowed access to knowledge of individual propeller speeds, would provide more clarity when designing and testing control algorithms.

Thirdly, a quadcopter that could be flown for longer would be helpful. While the cheap cost of the Cheerson CX-10 allowed for a fleet of 6 or more to be flown continuously without a battery charging bottleneck, building a data set for an individual quadcopter was very time consuming. The addition of a quadcopter with a longer battery life, or the ability to be connected to external power during flight, would streamline the process of data acquisition immensely.

APPENDIX A

APPENDIX

A.1 Additional Work

In addition to the work presented in the body of this report, a few avenues of research were pursued in the process of determining the ultimate direction of this investigation. A brief description of this work is provided below.

A.1.1 Comparisons to Other Turbulent Statistics

An investigation was made to see if any statistical properties of turbulence carried over into the statistics of the trajectory of the quadcopters. While a quadcopter is much more dense than the fluid in which it flies, it was thought that perhaps the thrust of the quadcopter and the ”brains” imparted by the control algorithm might make it behave statistically in some ways like a particle in turbulence. Two properties in particular were investigated: velocity structure functions and acceleration distributions.

Analysis of both of these quantities required estimates for the derivatives of position. Derivatives, and higher order derivatives in particular, are highly sensitive to noise, so some amount of care was needed in the estimation process. Since the use of only one camera made distinguishing between noise and real signal challenging, two different methods of derivative calculation were applied and compared.

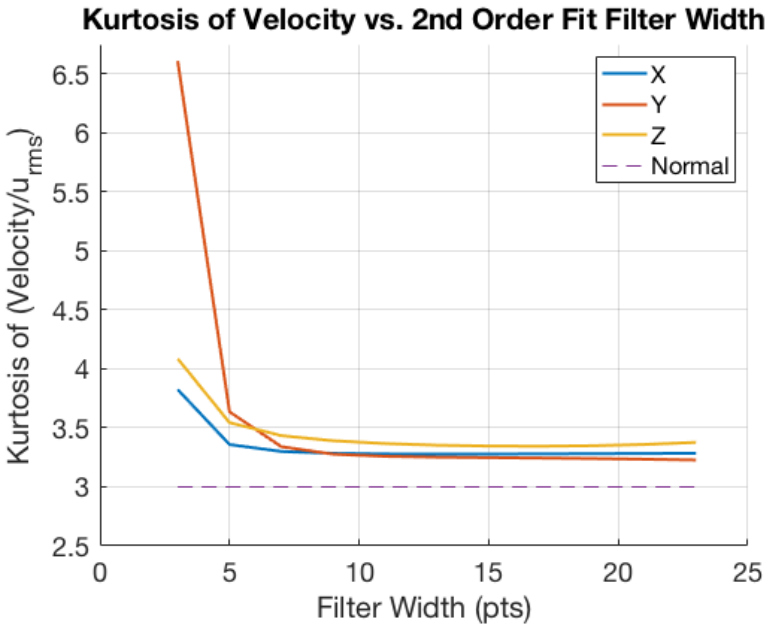

Figure A.1: Kurtosis of velocity using 2nd order fit for quadcopter in 13% turbulence intensity

The first method simply involved fitting parabolas to a window of a certain number of points, and then using the equations of the parabolas to calculate the derivatives. The choice of window size, also called filter width, can have a significant impact on the statistical properties of the derivatives. Since smaller windows are closer to the underlying data, but more susceptible to noise, striking the correct balance is key. A way to determine the proper filter width is to look at the kurtosis and variance of the values of the derivatives. For example, looking at the variance and kurtosis of velocity, the first derivative of position, (Figures A.2 and A.1), the kurtosis plateaus but the variance does not. The appropriate filter width was therefore taken to be where the kurtosis stopped decreasing, which corresponded to a filter width in the example of approximately 7 points. The same process was carried out for acceleration, but larger filter widths were needed before the kurtosis converged.

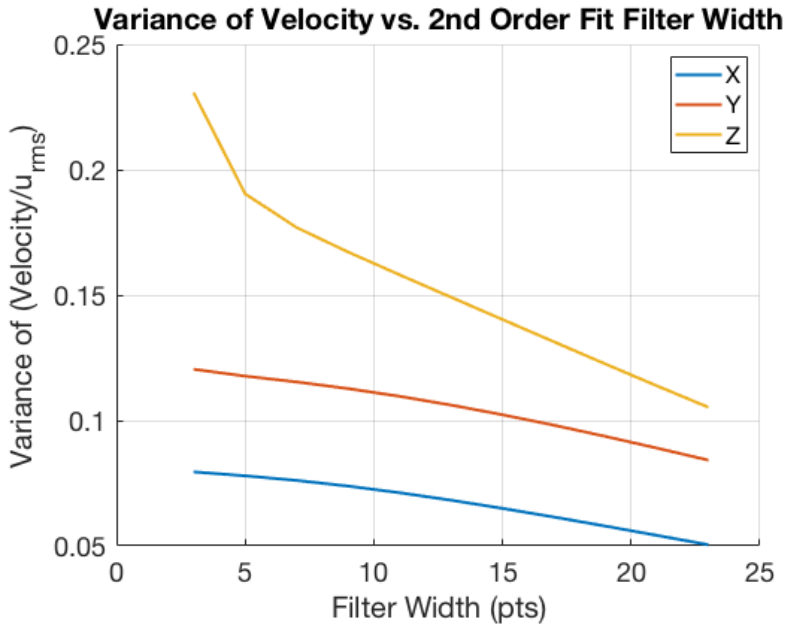

Figure A.2: Variance of velocity using 2nd order fit for quadcopter in 13% turbulence intensity

The second method involved fitting cubic splines to the position data and using the equations of the splines to calculate the derivatives. Matlab's function *csaps* was used, which takes as an argument the smoothing parameter p, which is between 0 and 1. A value of p closer to 0 prioritizes smoothness, and a value closer to 1 prioritizes matching the data points. From visual inspection, only values of the smoothing parameter greater than 0.99 fit the position data well enough to be considered. As seen in Figures A.3 and A.4, the kurtosis did not stop decreasing until p was very close to 1, and the variance increased continuously before diverging sharply at $p = 1$. The appropriate smoothing parameter was taken to be approximately 0.999, with small adjustments made in each case depending on the data. Across both methods the values for variance and kurtosis of both velocity and acceleration appeared to agree reasonably well for the chosen values relevant parameters.

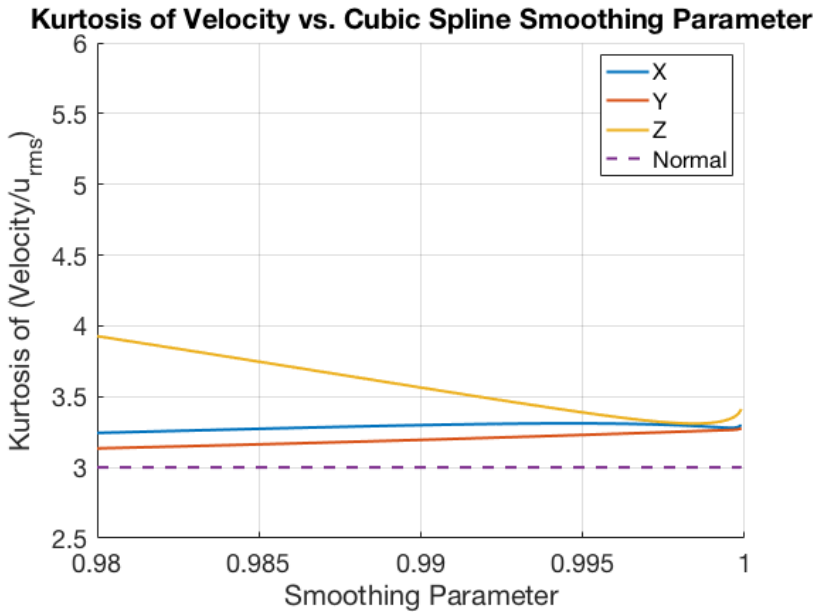

Figure A.3: Kurtosis of velocity using cubic spline fit for quadcopter in 13% turbulence intensity

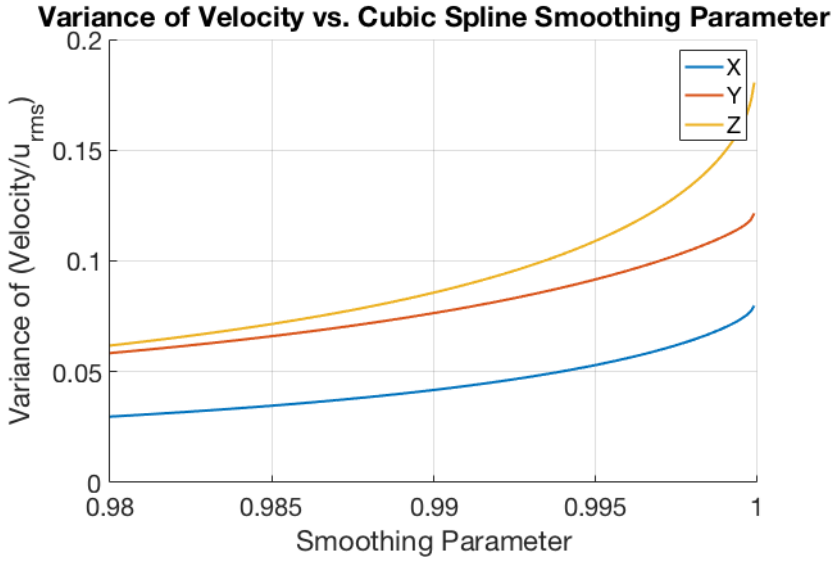

Figure A.4: Variance of velocity using cubic spline fit for quadcopter in 13% turbulence intensity

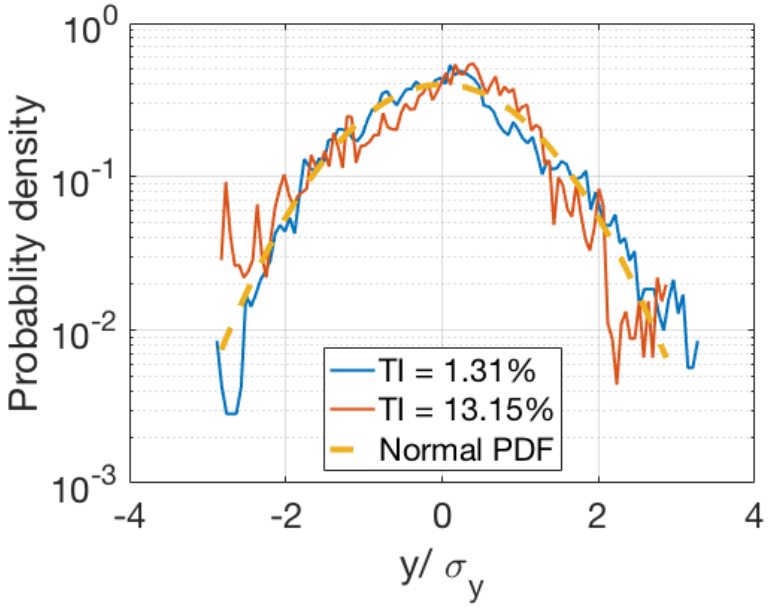

Figure A.5: Probability Density Function for Y-position with a Gaussian (normal) PDF for comparison.

An investigation was then done into the probability density functions (PDF) of position, velocity, and acceleration to see if any inherently turbulent statistics could be detected. As was already shown earlier with position, the variances of velocity and acceleration also increased with turbulence intensity. The PDF's of position, velocity, and acceleration are shown in Figures A.5, A.6, and A.7, and are normalized by the standard deviation to compare the shapes of the distributions for different turbulence intensities. Since these PDFs all appeared Gaussian, the search for intermittent statistics was inconclusive.

The velocity structure function in turbulence is a measure of how velocity differs as a function of spatial separation [2]. A similar analysis was carried out with the trajectory of the quadcopters, but using temporal separation instead. Under this definition, the structure function for velocity u is

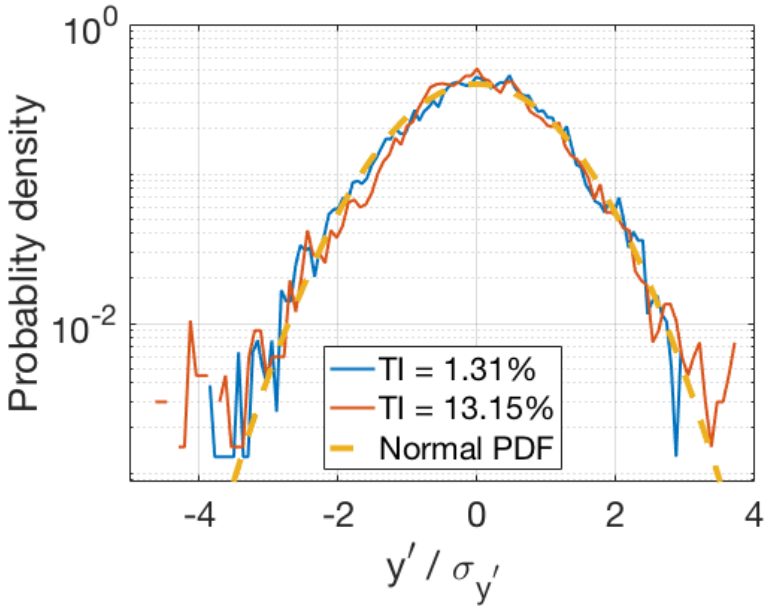

Figure A.6: Probability Density Function for Y-velocity with a Gaussian (normal) PDF for comparison.

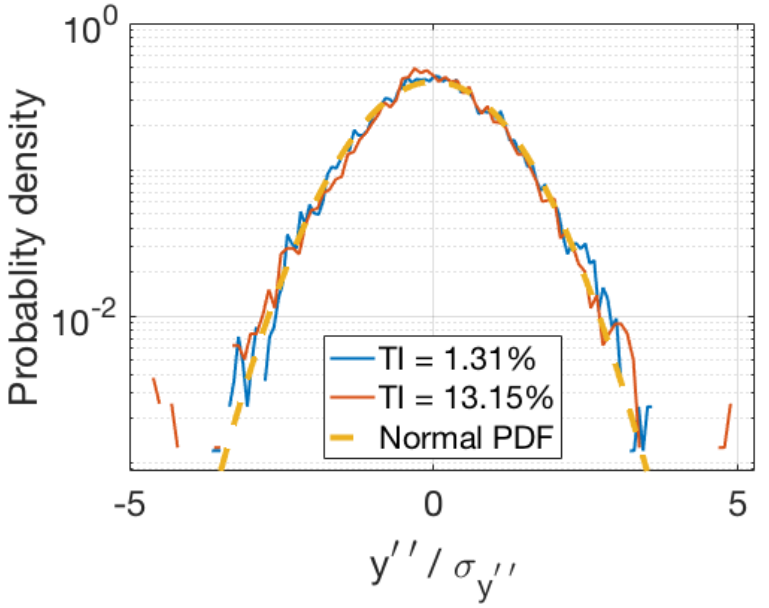

Figure A.7: Probability Density Function for Y-acceleration with a Gaussian (normal) PDF for comparison.

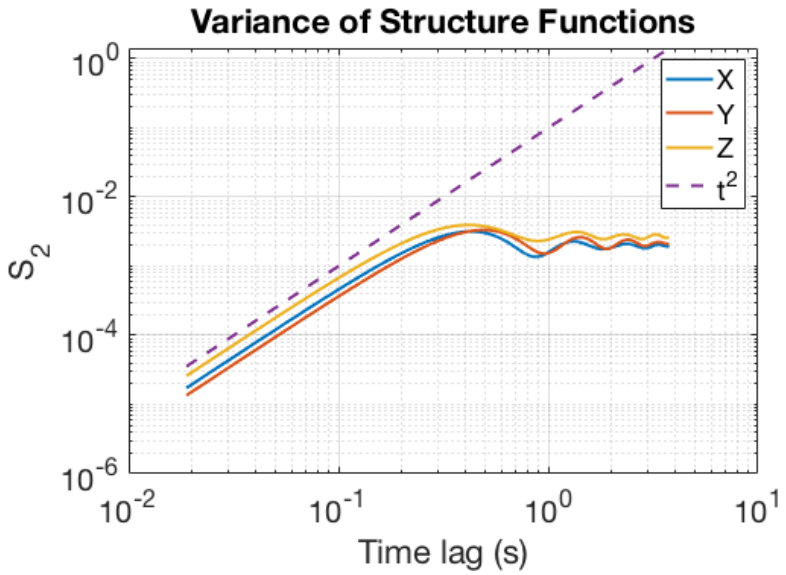

Figure A.8: Second-order velocity structure function vs. time lag for quadcopter in 13% turbulence intensity

$$\delta u(t, \tau) = u(t + \tau) - u(t) \tag{A.1}$$

where t is a given time and τ is the time lag. To get a measure of how time lag affects this function, the variance of δu for all t is calculated for different values of time lag. This is known as the second-order structure function, calculated as

$$S_2(\tau) = \left\langle \delta u^2 \right\rangle \tag{A.2}$$

A sample of this is shown in Figure A.8.

While the slopes of the beginning of these curves appeared to be the same as would be expected for a velocity structure function of a turbulent flow, this slope and the frequency of the oscillations were the same across all turbulence cases, both low and high. As a result, this measure was inconclusive with regards to whether or not turbulent statistics were demonstrated.

In order to have a chance at observing demonstrably turbulent statistics in quadcopter trajectory, it is suspected that as discussed earlier the response time of the quadcopter must be brought well below the eddy interception time.

A.1.2 Quadcopter Power Consumption

In addition to the effect of turbulence on a quadcopter's position, a preliminary investigation was done to analyze the effect of turbulence on a quadcopter's power consumption. Without the ability measure the power output of the battery, another method was needed. It was hypothesized that tracking the speed of the quadcopter's propellers would give a measure of how much energy the quadcopter was consuming during its flight. Since the propeller speeds could not be directly measured by the control system, they were instead tracked acoustically using a small microphone. By isolating the peaks in the audio spectrum, the propeller speeds over the course of flight could be estimated and used to compare the energy consumption of a quadcopter at different turbulence levels. Because of time constraints, work remains to be done with regards to validating the signal processing algorithm and applying it to the data from different turbulence cases. A sample audio spectrum can be seen in Figure A.9.

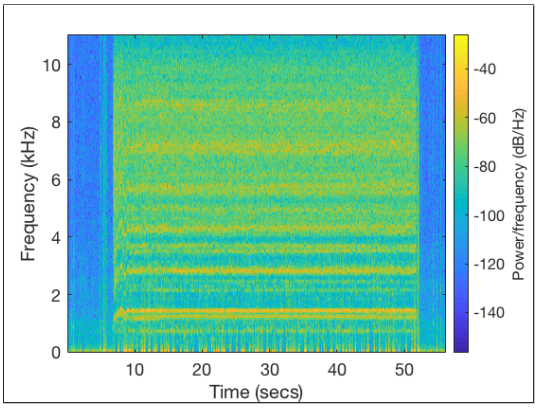

(a) Full spectrogram from a quadcopter flight. The background noise from the tunnel has been removed to isolate the signal of the quadcopter.

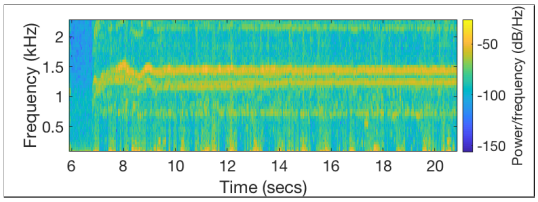

(b) Section of spectrogram from (a). In the region of interest, between approximately 1kHz and 1.6kHz, two distinct bands can be see which correspond to the front two propellers (lower frequency) and the rear two (higher frequency).

Figure A.9: Audio spectrum for quadcopter flight at TI = 13.15%. By comparing the location of the frequency bands shown in (b) for the same quadcopter at different turbulence intensities, a baseline estimate can be made as to whether flying in higher turbulence requires more or less energy.

BIBLIOGRAPHY

[1] 1903-The first flight. https://www.nps.gov/wrbr/learn/historyculture/thefirstflight.htm?utm_source=hootsuite. Accessed: 6/7/2018.

[2] Stephen B. Pope. *Turbulent Flows*. Cambridge University Press, 2000.

[3] Darryll J. Pines and Felipe Bohorquez. Challenges facing future micro-air-vehicle development. *Journal of Aircraft*, 43(2):290–305, 2006.

[4] Caitlin Powers, Daniel Mellinger, Alex Kushleyev, Bruce Kothmann, and Vijay Kumar. Influence of aerodynamics and proximity effects in quadrotor flight. *Proceedings of the Internation Symposium on Experimental Robotics*, 2012.

[5] J.H. McMasters and M. L.Henderson. Low speed single element airfoil synthesis. *Technical Soaring*, 6(2):1–21, 1980.

[6] US average annual wind speed at 30 meters. https://windexchange.energy.gov/maps-data/325. Accessed: 6/7/2018.

[7] Yanmin Chen, Yongling He, and Minfeng Zhou. Modeling and control of a quadrotor helicopter system under impact of wind field. *Research Journal of Applied Sciences, Engineering and Technology*, 6(17):3214–3211, 2013.

[8] Nguyen Khoi Tran, Eitan Bulka, and Meyer Nahon. Quadrotor control in a wind field. *International Conference on Unmanned Aircraft Systems*, pages 320–328, 2015.

[9] Sam Allison, He Bai, and Balaji Jayaraman. Modeling trajectory performance of quadrotors under wind disturbances. *AIAA SciTech Forum*, 2018.

[10] Fabrizio Schiano, Javier Alonso-Mora, Konrad Rudin, Paul Beardsley, Roland Y. Siegwart, and Bruno Sicilianok. Towards estimation and correction of wind effects on a quadrotor uav. *IMAV 2014:International Micro Air Vehicle Conference and Competition*, 2009.

[11] Nitin Sydney, Brendan Smyth, and Derek A. Paley. Dynamic control of autonomous quadrotor flight in an estimated wind field. *52nd IEEE Conference on Decision and Control*, 2013.

[12] B. Theys, G. Dimitriadis, T. Andrianne, P. Hendrick, and J. De Schutter. Wind tunnel testing of a vtol mav propeller in tilted operating mode. *2014 International Conference on Unmanned Aircraft Systems (ICUAS)*, 2014.

[13] Mark B.E. Boslough. Autonomous dynamic soaring platform for distributed mobile sensor arrarys. Technical report, Sandia National Laboratories, 2002.

[14] Michael J. Allen. Autonomous soaring for improved endurance of a small uninhabited air vehicle. *AIAA Aerospace Sciences Meeting and Exhibit*, 2005.

[15] Jack W. Langelaan. Long distance/duration trajectory optimization for small uavs. *AIAA Guidance, Navigation and Control Conference and Exhibit*, 2007.

[16] N.R.J. Lawrance, J.J. Acevedo, J.J. Chung, J.L. Nguyen, D. Wilson, and S. Sukkarieh. Long endurance autonomous flight for unmanned aerial vehicles. *Aerospace Lab*, 8, 2014.

[17] Jack W. Langelaan. Biologically inspired flight techniques for small and micro unmanned aerial vehicles. *AIAA Guidance, Navigation and Control Conference and Exhibit*, 2008.

[18] Chinmay K. Patel and Ilan Kroo. Control law design for improving uav performance using wind turbulence. *44th annual AIAA Aerospace Sciences Meeting and Exhibit*, 2006.

[19] National Academy of Sciences of the United States of America. *Learning to Soar in Turbulent Environments*, 2016.

[20] Jack W. Langelaan. Wind field estimation for small unmanned aerial vehicles. *Journal of Guidance, Control, and Dynamics*, 34(2):1016–1030, 2011.

[21] Ivar S. Ertesvag and Bjorn F. Magnussen. The eddy dissipation turbulence energy cascade model. *Combustion Science and Technology*, 159(1):213–235, 2000.

[22] Teach your PC to fly a mini-drone! `https://www.makehardware.com/2016/04/24/teach-your-pc-to-fly-a-mini-drone/`. Accessed: 6/7/2018.

[23] Katsuhiko Ogata. *Modern Control Engineering*. Pearson Education, 2010.

[24] OpenCV: Camera calibration. https://docs.opencv.org/3.4/dc/dbb/tutorial_py_calibration.html. Accessed: 6/7/2018.

[25] Kyunghwan Yoon and Zellman Warhaft. The evolution of grid-generated turbulence under conditions of stable thermal stratification. *Journal of Fluid Mechanics*, 215:601–638, 1990.

[26] L. Mydlarski and Z. Warhaft. Passive scalar statistics in high-peclet-number grid turbulence. *Journal of Fluid Mechanics*, 358(2):135–175, 1998.

[27] Mohamad Kazemi Esfeh. *Analytical and Experimental Investigation About Heat Transfer of Hot-Wire Anemometry*. INTECH, 2012.

[28] H.H. Bruun. *Hot-Wire Anemometry: Principles and Signal Analysis*. Oxford University Press, 1995.

[29] Physics demonstrations: vortex cannon! https://skullsinthestars.com/2012/08/28/physics-demonstrations-vortex-cannon/. (Accessed: 6/7/2018).